Nanoscale

REVIEW

View Article Online
View Journal | View Issue

Cite this: *Nanoscale*, 2019, **11**, 13181

Two-dimensional layered materials: from mechanical and coupling properties towards applications in electronics

Hao Zhan, Dan Guo * and GuoXin Xie *

With the increasing interest in nanodevices based on two-dimensional layered materials (2DLMs) after the birth of graphene, the mechanical and coupling properties of these materials, which play an important role in determining the performance and life of nanodevices, have drawn increasingly more attention. In this review, both experimental and simulation methods investigating the mechanical properties and behaviour of 2DLMs have been summarized, which is followed by the discussion of their elastic properties and failure mechanisms. For further understanding and tuning of their mechanical properties and behaviour, the influence factors on the mechanical properties and behaviour have been taken into consideration. In addition, the coupling properties between mechanical properties and other physical properties are summarized to help set up the theoretical blocks for their novel applications. Thus, the understanding of the mechanical and coupling properties paves the way to their applications in flexible electronics and novel electronics, which is demonstrated in the last part. This review is expected to provide in-depth and comprehensive understanding of mechanical and coupling properties of 2DLMs as well as direct guidance for obtaining satisfactory nanodevices from the aspects of material selection, fabrication processes and device design.

Received 28th April 2019,
Accepted 13th June 2019

DOI: 10.1039/c9nr03611c

rsc.li/nanoscale

1. Introduction

2DLMs refer to ultrathin nanofilms (thickness <100 nm) consisting of atomic layers linked by weak van der Waals interaction. Graphene is a typical single-layer material with carbon

State Key Laboratory of Tribology, Tsinghua University, Beijing, 100084, China. E-mail: guodan26@tsinghua.edu.cn, xgx2014@tsinghua.edu.cn

Hao Zhan

Hao Zhan obtained his B. S. from Huazhong University of Science and Technology in 2017. He is currently a PhD candidate in State Key Laboratory of Tribology of Tsinghua University, and his research interest is in the mechanical and coupling properties of 2D materials.

Dan Guo

Dan Guo received the master and Ph.D. degrees in Engineering Mechanics, from Xi'an Jiaotong University and Tsinghua University in China. Now she is a professor in State Key Laboratory of Tribology of Tsinghua University. Her present research interests are mainly focused on the mechanical properties of nanomaterials, interface behavior of nanoparticles. She has been an author of more than 150 papers. She awarded the First Class, the Second Class of Award for Natural Science in Ministry of Education of China, and the second Class of Award for National Natural Science of China in 2011, 2014 and 2018, respectively.

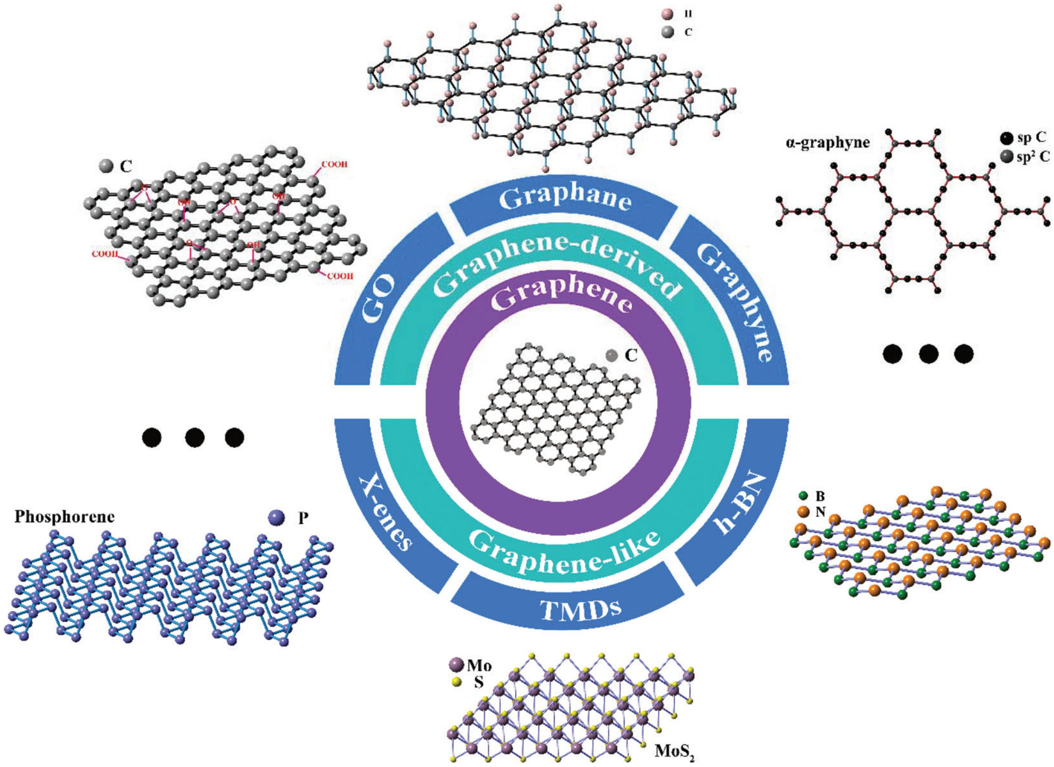

Fig. 1 Types and structures of 2DLMs.

atoms arranged in a honeycomb lattice.[1] Due to the unique physical properties such as quantum Hall effect,[2] quantum confinement,[3] ultrahigh Young's modulus,[4] extremely high mobility[5] and large specific surface area,[6] significant progress has been made to enable its applications in electronics,[7–11] nanomechanical systems,[12–15] energy systems,[16–18] reinforced composites[19–27] and environmental protection.[28] However, the absence of a bandgap in graphene hinders its applications in some fields. Even though functionalization of hydrogen,[29,30] an electrical field[31] and external deformation[32,33] have been reported to modulate the graphene bandgap from zero to a limited value, the opened bandgap is so small that graphene still cannot be used as electrical switches for digital transistors.

Inspired by graphene, more attentions are turned to other 2DLMs (shown in Fig. 1). Graphene-derived materials are obtained from graphene by introducing functional groups[34,35] or sp hybridized carbon atoms,[36,37] including graphene oxide (GO), graphane and graphyne family. On the other hand, graphene-like materials are novel 2D materials that have a similar honeycomb structure, such as silicene, phosphorene, hexagonal boron nitride (h-BN), transition metal dichalcogenides (TMDs) and transition metal carbides (TMCs). Significantly, the weaker out-of-plane van der Waals interaction than in-plane covalent bonding induces the direct exfoliation of single-layer nanosheet and mechanical stacking of their heterostructures,[38] thus providing another direction for designing novel nanodevices with excellent performances. Recent advances[39–47] in these materials and their heterostructures have also confirmed their excellent properties comparable to graphene.

However, the rise of 2DLMs is no doubt attributed to the excellent mechanical properties absent in their corresponding bulk materials. Since external loads are inevitable in the

GuoXin Xie

Guoxin Xie received his doctoral degree at Tsinghua University, China, in 2010. After that, he worked at State Key Laboratory of Tribology, Tsinghua University, China and Royal Institute of Technology, Sweden for postdoctoral research from 2010 to 2014. Since 2014, he has worked at Tsinghua University as an Associate Professor. His research interests include solid lubrication, electric contact lubrication, thin film lubrication, etc. *He has published more than 60 papers in international journals. He won several important academic awards, such as Chinese Thousands of Young Talents, the Excellent Doctoral Dissertation Award of China, and Ragnar Holm Plaque from KTH, Sweden.*

process of manufacture and use,[48–50] 2DLMs with a higher strength and flexibility will be more preferable for nanodevices. Even sometimes there is a need to design devices with specific and controllable mechanical properties by defect engineering[51,52] or functionalization.[53] Besides, the electronic properties of 2DLMs often vary with different external load types and load sizes,[54–60] making it possible to tune the electronic properties for suitable applications. 2DLMs can also be used as ideal testbeds for fundamental studies of mechanics under extreme strains with the help of molecular dynamics (MD) and density functional theory (DFT).[4,61,62] Therefore, the understanding of mechanical properties and behaviour of 2DLMs is urgently required for not only helping design nanodevices with satisfactory performance and service life, but also comprehending fundamental mechanics. On the other hand, the coupling properties between mechanical and other physical properties are not only helpful to tailor the mechanical properties of 2DLMs, but also intriguing for potential novel applications in electronics.

In this review, experimental and simulation methods exploring the mechanical properties and behaviour of 2DLMs are firstly summarized. Then, the elastic properties and failure mechanisms of 2DLMs are discussed and summarized for deeper understandings of the reasons for their unique mechanical properties and behaviour. For further tuning of the mechanical properties of 2DLMs, the factors that can greatly influence the mechanical properties and behaviour are deeply analyzed in the third part. Then, recent progresses of the coupling properties between mechanical and other physical properties (electrical, optical, thermal and structural) are covered. At last, flexible electronics based on mechanical properties and novel electronics based on coupling properties are demonstrated. The basic framework of this review is schematically shown in Fig. 2. Though some other reviews[63–68] on similar topics are available, there are some apparent differences between the present review and those reviews. Castellanos-Gomez *et al.*[63] mainly focused on the static mechanical properties of 2DLMs and the dynamics of mechanical resonators based on 2DLMs. Liu *et al.*[64] summarized the mechanical properties of different 2DLMs and their heterostructures and discussed their applications as resonators. Papageorgiou *et al.*[67] reviewed the mechanical properties of graphene and graphene-based nanocomposites. Androulidakis *et al.*[68] systematically analysed the nanoindentation method and the mechanical properties of 2DLMs and heterostructures as well as their interfaces. However, it is insufficient to merely study the mechanical properties of 2DLM for their practical applications, especially in electronics where the relationship between the mechanical properties and other physical properties (*e.g.*, electrical, optical and thermal) should be taken into consideration. Recently, Akinwande *et al.*[65] introduced the basic progress of the thermomechanical and electromechanical properties of 2DLMs. Kim *et al.*[66] listed some applications of the coupling properties, including strain engineering, piezoelectricity and strain sensors. The differences of the specific arrangements between this review and the two reviews in ref. 65 and 66 can be summarized as the following points. Firstly, the experimental and theoretical characterization methods are well categorized (such as the development history of various experimental methods and the main calculation formula) with their different properties from each other, which is very helpful for the readers to understand, choose and use these methods in a fast and simple way. Secondly, the elastic properties and the failure mechanisms of a wide range of 2DLMs are all deeply analyzed from the basic structures (chirality, bond types, bond strength and buckled structures) and influence factors (defects and others), offering a systematic and profound insight into their mechanical properties and behaviour. Thirdly, recent developments in both theories (electromechanical properties, optomechanical properties, themomechanical properties and strain-induced phase transition) and applications (electronics based on piezoresistive property, piezoelectric property and strain-enhanced photoabsorption) are all discussed, which will provide coherent inspiration for the readers interested in the electronics based on 2DLMs.

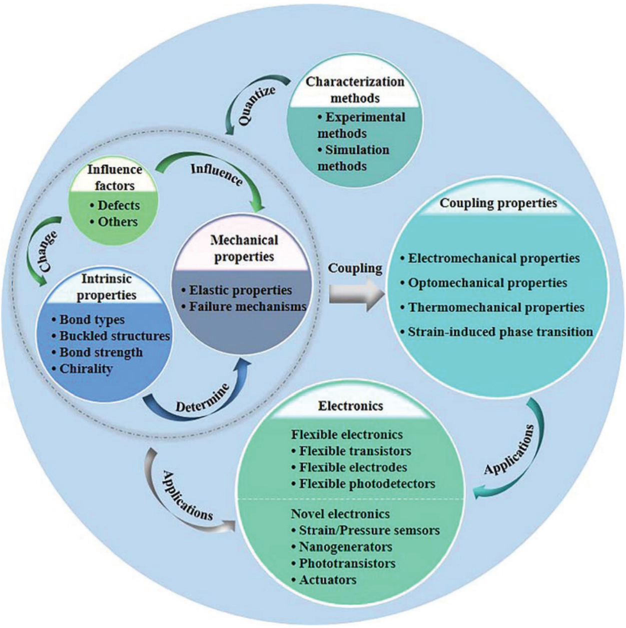

Fig. 2 Schematic diagram of the framework of this review.

2. Characterization methods

In recent years, huge efforts have been made to develop effective mechanical characterization methods based on experiments or computational simulations. Two strategies (shown in Fig. 3) have been adopted in experimental methods: indirect testing and direct testing. Indirect testing denotes that mechanical parameters can be extracted from static or dynamic deformation of 2D beams or membranes on the basis of continuum theory. Thus, the mechanical properties of 2DLMs can be extracted from the elastic stiffness. Indirect testing can be divided into resonator-based methods where

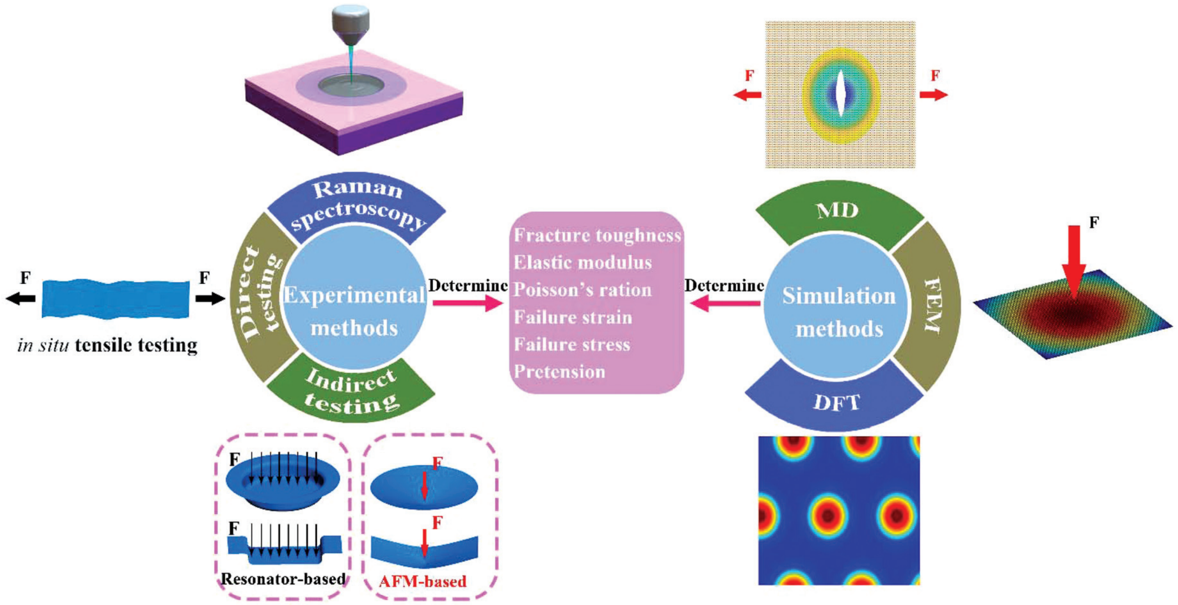

Fig. 3 Schematic illustration of mechanical characterization methods for investigating the mechanical properties and behaviour of 2DLMs.

the load is uniform pressure[12,69] and AFM-based methods where the load is a point load.[4] On the other hand, direct testing gives the opportunity for direct measurement of mechanical properties and observation of mechanical behaviour within scanning electron microscopy (SEM) or transmission electron microscopy (TEM).[70–75] Besides, Raman spectroscopy can be utilized to directly map the relationship of lattice deformation and external strain in a non-destructive manner, which is very useful in the experiments of strain engineering and related applications. As for the simulation methods, though some simple and multi-scale issues can be solved by finite element model (FEM), the continuum mechanics hinder its further application at the nanoscale. Since MD and DFT have the ability of accurately simulating the mechanical behaviour during deformation from the atomic scale, these methods are effective routes for predicting the mechanical properties and investigating the nature behind mechanical behaviour. Since the strain energy density is normalized by the area of quasi 2D materials, it is more suitable to describe the mechanical properties by 2D constants (2D modulus and strength) instead of 3D constants (3D modulus and strength).[4] However, 3D constants obtained by dividing 2D constants with the interlayer spacing or thickness are still indispensable for the comparison to corresponding bulk materials or other materials.

2.1 Experimental methods

In 2007, McEuen *et al.*[12] systematically studied the vibrations of resonators based on single- and multilayer graphene and developed the beam dynamic method. However, they[76] thought it was nontrivial to determine the absolute amplitude of the motion, thus developing the beam bending method. In 2008, a pressurized blister method was further developed when they found that a monolayer graphene membrane was impermeable to standard gases.[69] Meantime, Lee *et al.*[4] established the circular membrane indentation method and found graphene was the strongest material ever measured. While in 2010, Wong *et al.*[77] modelled the electrostatic deflection behaviour by combining analytical formulations and FEM, thus proposing the electrostatic deflection method. Based on the pressurized blister method, Lee *et al.*[78] further developed a rapid and non-destructive method by using Raman spectroscopy. Though *in situ* tensile testing was originally used for measuring the mechanical properties of carbon nanotubes,[79,80] it has been also reported for 2DLMs including graphene,[70,71,73] h-BN,[71] GO nanosheets,[72,75] MoS_2[73] and $MoSe_2$[74] since 2014. Very recently, Davidovikj *et al.*[81] developed a nonlinear dynamic characterization method (or called circular membrane dynamic method) on the basis of the exact relation between the nonlinear response and the resonator's material properties.

Even though these experimental methods have been widely used in determining the mechanical properties of 2DLMs, every method has its own advantages and disadvantages to be distinguished. In the beam dynamic method, E and T significantly depend on the effective spring constant k, and thus the measurement of resonance frequencies and amplitudes of the motions become critical. The beam bending method enables the measurements of E along arbitrary crystal orientations, which is very practical for anisotropic 2D materials.[82,83] While circular membrane indentation method measures the average mechanical parameters of all orientations. Thus, this method is more suitable for isotropic 2DLMs, such as graphene,[4,50] MoS_2[84,85] and WS_2.[84] As for the pressurized blister method, it has only been used for the measurement of Young's modulus and pretension of graphene. Whether it could be suitable for other 2DLMs is unclear. Though no disturbances to the mor-

Table 1 Experimental methods for determining the mechanical properties of 2DLMs

Loading features	Determinable mechanical properties	Method	Applicable conditions	Expressions of stiffness			Ref.
				Bending	Pretension	Stretching	
Static point loading	E^{2D}, T^{2D}	(1)	2D beam	$\frac{Ew\pi^4t^3}{6L^3}$	$\frac{T\pi^2}{2L}$	$\frac{Ew\pi^4t}{8L^3}$	76, 82, 83, 87 and 88
	E^{2D}, T^{2D}, $\sigma_m{}^{2D}$	(2)	2D circular membrane	$\frac{4\pi E^{2D}t^2}{3(1-\nu^2)R^2}$	πT^{2D}	$\frac{q^3E^{2D}}{R^2}$	4, 50, 85, 91–93
Dynamic uniform loading	E^{2D}, T^{2D}	(3)	Conductive beam	$\frac{30.78Ewt^3}{L^3}$	$12.32\frac{T}{L}$	—	12 and 76
	E^{2D}, T^{2D}	(4)	Conductive circular membrane	—	$1.56\pi T^{2D}$	$\frac{Et\pi q}{R^2}$	81
Static uniform loading	E^{2D}, T^{2D}	(5)	Conductive circular membrane	—	$4\pi T^{2D}$	$\frac{8\pi E^{2D}}{3(1-\nu)R^2}$	81 and 86
	K_{IC}, E^{2D}, $\sigma_m{}^{2D}$, ε_m	(6)	2D beam	—	—	—	71–75
Static and dynamic uniform loading	E^{2D}, T^{2D}	(7)	Square/circular membrane of graphene	—	$4c_1T^{2D}$ (square); $4\pi T^{2D}$ (circular)	$\frac{16c_2Et}{W^2(1-\nu)}$ (square); $\frac{8\pi Et}{3R^2(1-\nu)}$ (circular)	69, 89 and 90

Note: (1) denotes beam bending method; (2) denotes circular membrane indentation method; (3) denotes beam dynamic method; (4) denotes circular membrane dynamic method; (5) denotes electrostatic deflection method; (6) denotes *in situ* tensile testing; (7) denotes pressurized blister method. K_{IC} is critical stress intensity factor, ε_m is failure strain.

phology of nanosheets will occur *via* a non-contact process in electrostatic deflection method, this method cannot be used to determine the breaking strength of nanosheets because of the limit of low applied pressure.[86] Circular membrane dynamic method provides access to Young's modulus and pretension from high-frequency resonance measurements, allowing for the usage of very small actuation forces. The results of *in situ* tensile testing highly depend on the resolution and precision of nanomechanical testing device. Raman spectroscopy is mainly employed to determine the deformation of crystal lattice. Though the AFM-based methods yield stress concentration near the AFM tip, suitable for all 2D materials as well as relatively simple experiments and data processing make them more popular than the resonator-based methods. But the AFM-based methods are all operated under relative large static loading which trends to destroy 2D materials, while the resonator-based methods allow for the dynamic measurements under small driving force. *In situ* tensile testing is mainly used to investigate mechanical behaviour during deformation. All these experimental methods mentioned above will be discussed in chronological order of development and the summary of these methods can be obtained in Table 1.

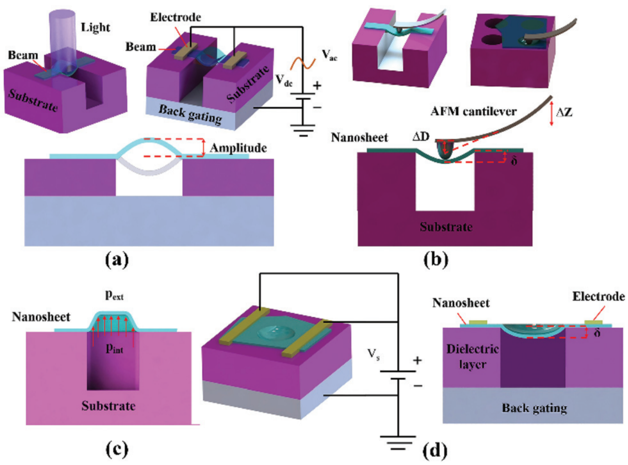

Fig. 4 (a) Schematic of beam dynamic method. (Left inset) Light-actuated motions. (Right inset) Electric-actuated motions. (b) Schematic of AFM-based methods, including beam bending method (left inset) and circular membrane indentation method (right inset). Resulting deflection δ is determined by subtracting AFM cantilever deflection ΔD from scanning piezo displacement ΔZ. (c) Schematic of pressurized blister method. (d) Schematic of electrostatic deflection method.

2.1.1 Beam dynamic method.

In this method, vibrations of resonators are usually actuated by either optical (left inset in Fig. 4(a)) or electrical (right inset in Fig. 4(a)) modulation, thus the fundamental resonance frequency of resonators under tension can be derived from:[76]

$$f_0 = A\sqrt{\frac{Et^2}{\rho L^4}+\frac{T}{3.4\,\mathrm{mL}}} \tag{1}$$

where $A = 1.03$ is the clamping coefficient of doubly clamped beams,[12] E is Young's modulus, ρ is the density of the beam, T is the pretension, m is the effective mass, and t and L are the thickness and length of the beam, respectively. Combining with the relation $m = 0.735\rho wLt$ and $f_0 = (1/2\pi)(k/m)^{1/2}$, where w and k are the width and the effective spring constant of the beam, k could be solved by the following equation:[76]

$$k = 30.78Ew(t/L)^3 + 12.32\frac{T}{L}. \tag{2}$$

Apparently, beam dynamic method is a non-contact method where both E and T can be derived by a curve fit of eqn (2).

2.1.2 Beam bending method. Beam bending method (shown in Fig. 4(b) (left inset)) related to continuum mechanics[87] provides effective measurements on Young's modulus and pretension of a doubly clamped beam. The dependence between load and displacement can be explained by the spring stiffness consisting of bending, stress and stretching components for a doubly clamped beam. Therefore, the relationship between the deformation and the load can be described by the expression:[88]

$$\begin{aligned} F &= k_{\text{bending}}\delta + k_{\text{stress}}\delta + k_{\text{stretching}}\delta^3 \\ &= \frac{Ew\pi^4}{6}\left(\frac{t}{L}\right)^3\delta + \frac{\sigma_0 w\pi^2}{2}\left(\frac{t}{L}\right)\delta + \frac{Ew\pi^4}{8}\left(\frac{t}{L^3}\right)\delta^3 \end{aligned} \tag{3}$$

where E is the Young's modulus; w, t and L are the width, thickness and length of beam, respectively; σ_0 is the intrinsic stress; F is the load applied in the beam center; δ is the resulting beam deflection. The first and second terms in eqn (3) correspond to linear elastic response of bending and intrinsic stress respectively, while the third term represents nonlinear elastic response of stretching under large displacement.

Thus the Young's modulus and intrinsic stress σ_0 of 2D beams can be extracted from the fits of eqn (3). Significantly, pretension T ($T = \sigma_0 wt$) was used instead of intrinsic stress σ_0 in some studies,[76,82,83,87] then the effective spring constant of beam within the linear elastic response can be used for the extraction of E and T.[76,87,88]

2.1.3 Pressurized blister method. As shown in Fig. 4(c), a microchamber is fabricated as testing platform by depositing graphene over a pre-etched substrate with square or circular wells. Then uniform pressure can be applied on the surface of graphene through the pressure differences inside and outside the chamber. For a square membrane, the relationship between pressure difference and deflection can be expressed as:[69]

$$\Delta p = \frac{4\delta}{W^2}\left(c_1 T^{2\text{D}} + \frac{4c_2 Et\delta^2}{W^2(1-\nu)}\right) \tag{4}$$

where Δp is the pressure difference, δ is the central deflection, W is the side length, $T^{2\text{D}}$ is 2D pretension in the membrane, t is the thickness, E is Young's modulus, ν is Poisson's ratio, and c_1 and c_2 are equal to 3.393 and $(0.8 + 0.062\nu)^{-3}$, respectively. While for a circular membrane, there is also a similar expression between pressure difference and deflection.[89,90] To determine the Young's modulus of graphene *via* eqn (4), the pretension term is assumed to be negligible. Besides, the fundamental frequency of a square membrane under uniform tension without considering the bending rigidity is determined by:[69]

$$f = \sqrt{\frac{T^{2\text{D}} + T^{\text{P}}}{2\,\text{m}W^2}} \tag{5}$$

where f is the resonance frequency that can be actuated optically and detected optically by interferometry,[12] T^{P} is the pressure-induced tension, and m is the mass per unit area which can be obtained by theoretical estimation or dynamic measurements. Therefore, pretension can be extracted under the condition of $\Delta p = 0$.

2.1.4 Circular membrane indentation method. Circular membrane indentation method (right inset in Fig. 4(b)) is to some extent consistent with beam bending method, but 2D nanosheets are prepared into circular suspended membranes instead of rectangular strips. The force-displacement behaviour can be described by the expression[85,91]

$$\begin{aligned} F &= k_{\text{bending}}\delta + k_{\text{pretension}}\delta + k_{\text{streching}}\delta^3 \\ &= \left[\frac{4\pi E^{2\text{D}}}{3(1-\nu^2)}\left(\frac{t^2}{R^2}\right)\right]\delta + \left(\pi T^{2\text{D}}\right)\delta + \left(\frac{q^3 E^{2\text{D}}}{R^2}\right)\delta^3 \end{aligned} \tag{6}$$

where F is applied force, δ is the deflection at the membrane center, $E^{2\text{D}}$ is 2D elastic modulus (in-plane stiffness), $T^{2\text{D}}$ is 2D pretension, ν is Poisson's ratio, R is membrane radius, and $q = 1/(1.0491 - 0.1462\nu - 0.15827\nu^2)$ is a dimensionless constant. Similarly, the deformation consists of linear elastic response under small loads and nonlinear elastic response under larger loads. Thus the effective spring constant of 2D nanosheets under small loads could also be used for the extraction of E and T.[85,92,93] When taking the size of the indenter into consideration, the force-displacement equation could be further modified.[50]

In addition to Young's modulus and pretension, breaking strength can also be derived from the model of a clamped circular membrane under a point load. Thus, the maximum stress can be derived by[4]

$$\sigma_{\text{m}}^{2\text{D}} = \left(\frac{FE^{2\text{D}}}{4\pi r}\right)^{\frac{1}{2}} \tag{7}$$

where $\sigma_{\text{m}}^{2\text{D}}$ is maximum stress and r is indenter radius.

2.1.5 Electrostatic deflection method. Electrostatic deflection method (shown in Fig. 4(d)) based on parallel-plate capacitor approximation enables a non-contact approach of measuring in-plane stiffness of 2DLMs. Firstly, the suspended circular membranes are driven to deform by uniform electrostatic force between substrate and nanosheet. Then, the maximum center-point deflection is obtained by AFM scanning[77] or interferometric profilometry[86] to extract the in-plane stiffness from force-deflection curve fit. Since the electrostatic force between nanosheet and gating chip can be accurately evaluated.[81,86] Besides, the deformation of electrostatically driven membranes could be modelled as clamped circular plates under uniform pressure, thus giving the relationship between F and δ by[81,86]

$$F = 4\pi T^{2\text{D}}\delta + \frac{8\pi E^{2\text{D}}}{3(1-\nu)R^2}\delta^3 \tag{8}$$

where $T^{2\text{D}}$ and $E^{2\text{D}}$ are 2D pretension and 2D elastic modulus, respectively; δ is the maximum center-point deflection; ν is Poisson's ratio; R is membrane radius.

2.1.6 Raman spectroscopy. Raman spectroscopy based on lattice dynamics is a rapid and non-destructive method in investigating the mechanical properties and behaviour of

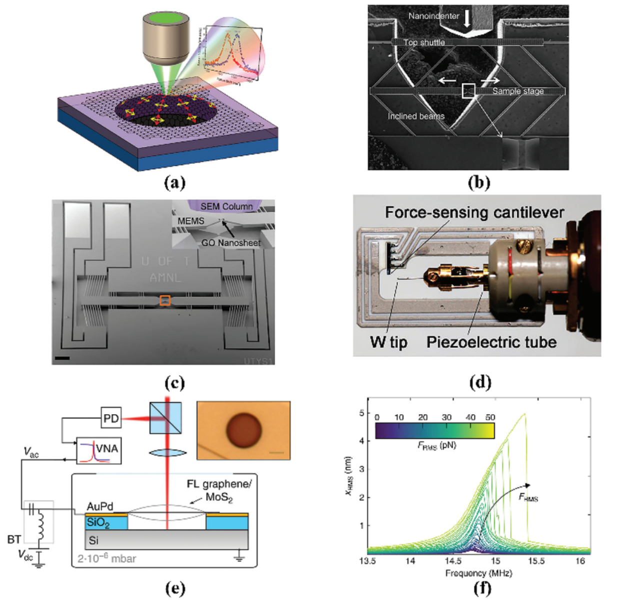

Fig. 5 (a) Raman spectroscopy for determining the Young's modulus of pressurized graphene. (b) SEM image showing the *in situ* tensile testing with a nanomechanical testing device. (c) SEM image of the integrated nanomechanical testing device possessing two symmetrical thermal actuators (scale bar: 200 μm). (d) Nanomechanical testing device combining a force-measuring system and a high-precision piezoelectric tube-driven nanomanipulating system. (e) Schematic of the measurement setup. Inset: An optical image of a few-layer graphene nanodrum (scale bar: 2 μm). (f) Frequency response curves of the calibrated root-mean-square (RMS) motion amplitude for increasing electrostatic driving force. Reprinted with permission from ref. 78. Copyright 2012 American Chemical Society. Reprinted with permission from ref. 70. Copyright 2014 Springer Nature. Reprinted with permission from ref. 72. Copyright 2015 American Chemical Society. Reprinted with permission from ref. 71. Copyright 2015 American Chemical Society. Reprinted with permission from ref. 81. Copyright 2017 Springer Nature.

2DLMs. By analyzing the frequency difference of reflected photons and incident photons due to Raman scattering, the information of crystal lattice can be acquired. Therefore, strain induced lattice deformation can be directly and accurately displayed in Raman shift, and the relationship between corresponding stress and Raman shift can be obtained on the basis of lattice mechanics and solid mechanics. So far, Raman spectroscopy has been used to probe local strain in graphene,[94–96] MoS_2,[97] WSe_2 [98] and black phosphorus.[99] By combining Raman spectroscopy and numerical simulation (shown in Fig. 5(a)), the Young's modulus of graphene even has been measured.[78] Since the applied strain can be accurately detected in Raman shifts, some studies[100–102] have further employed Raman spectroscopy to investigate the relationship between external stain and intrinsic physical properties of 2DLMs in strain engineering.

2.1.7 *In situ* tensile testing. In the method of *in situ* tensile testing, nanomechanical testing device with high resolution and precision is the most critical part responsible for the exertion of external loads and the information collection of deformation. For first measuring the fracture toughness of graphene, a quantitative InSEM nanoindenter (Agilent Technologies, Oak Ridge, Tennessee) (shown in Fig. 5(b)) was employed based on a spring-like "push–pull" mechanism.[70] However, the motion of nanoindenter head was likely to cause slippage at contact points and misalignment of the shuttles with the nanoindenter axis, thus the device was further improved by replacing nanoindenter-driven motion with voltage-driven motion (shown in Fig. 5(c)).[72,75] When a voltage was applied, the two actuation shuttles would move in opposite directions. Besides, a side-entry AFM-TEM holder (Nanofactory Instruments AB) combining a force-measuring system and a high-precision piezoelectric tube-driven nanomanipulating system (shown in Fig. 5(d)) was used for measuring the fracture toughness of multilayer graphenes and boronitrenes.[71] The W tip was retracted at a constant speed with the direction perpendicular to the crack. So far, *in situ* tensile testing has been used for determining fracture toughness, elastic modulus, failure stress and failure strain as well as investigating fracture behaviour of several 2DLMs.

2.1.8 Circular membrane dynamic method. Very recently, a circular membrane dynamic method (shown in Fig. 5(e)) has been developed on the basis of the nonlinear dynamic response (shown in Fig. 5(f)) of electrostatically driven circular resonators.[81] For determining the mechanical properties of resonators, the applied electrostatic force amplitude F_{el} can be firstly solved.[81] Consequently, the cubic spring constant k_3 representing the dynamic nonlinear behaviour of resonators can be derived from the curve fit by finding the positive real roots x^2 of:[81]

$$\xi^2 F_{el}{}^2 = (\omega^2 c^2 + m_{eff}{}^2(\omega^2 - \omega_0{}^2)^2)x^2 - \frac{3}{2}m_{eff}(\omega^2 - \omega_0{}^2)k_3 x^4 + \frac{9}{16}k_3{}^2 x^6 \tag{9}$$

where w_0 is the resonance frequency, m_{eff} (equal to 0.269 m, m is the mass of memebrane) is the effective mass of membrane, c is the damping constant, $\xi = 0.432$ is the correction factor, x is the deflection of the membrane's center, and ω is the driving frequency. Note that f_0 (fundamental resonance frequency) is extracted from the linear response curves at low-driving powers, hence the T^{2D} (2D pretension) is available by $T^{2D} = 0.69\pi^2 f_0{}^2 R^2 \rho$ t where ρ is the density of membrane and t is the thickness of membrane. To determine the Young's modulus of membrane, the nonlinear force-deflection relationship derived from the deformation potential energy is needed and described by:

$$F = k_1 x + k_3 x^3 = 1.56\pi T^{2D} x + \frac{Et\pi q}{R^2}x^3 \tag{10}$$

where $q = 1/(1.269 - 0.976\nu - 0.269\nu^2)$ is a dimensionless constant. By rewriting the coefficient of second term in eqn (10), Young's modulus E is equal to $R^2 k_3/\pi qt$.

2.2 Simulation methods

Simulation methods are of great importance to the study of not only determining the mechanical properties of 2DLMs, but also simulating their mechanical behaviour that cannot be

Table 2 Properties of simulation methods

Method	Principle	Simulation size	Applicable condition	Bandgap description	Determinable parameters
FEM	Continuum mechanics	Macro scale	Simple/Multi-scale issues	no	σ, ε
MD	Newton's motion equations	Thousands of atoms	Complicated issues	no	E, ν, σ, ε
DFT	Quantum mechanics	Hundreds of atoms	Simple issues	Yes	

realized by experimental methods above. Typically, these simulation methods can be classified as conventional modelling based on continuum mechanics (such as FEM) and atomic modelling (such as MD and DFT). Though FEM has been employed to probe the mechanical properties of 2DLMs in some studies,[62,71,103–106] there is still a doubt whether continuum mechanics are suitable for atomically-thin membranes. In contrast, MD and DFT are more effective and applicable methods in this area. But it should be noted that the numbers of atoms handled in DFT is much less than that in MD. In other words, more computational costs will be necessary to investigate some complicated mechanical problems involving more atoms *via* the DFT calculations. On the other hand, the ability to depict energy band structure makes DFT widely adopted to study the relationship between external loading and internal band structure changes, which promotes great development of strain engineering in the 2D materials. The basic properties of these simulation methods are summarized in Table 2.

Usually, FEM is combined with experiments to estimate the mechanical properties of 2DLMs. During simulation, the modelling of 2DLMs in FEM based micromechanical approach is critical in guaranteeing the validity of the results. For example, atomic layer of 2DLMs is modelled as isotropic membrane under external load or pressure,[105,106] but this is only applicable in some axisymmetric materials. Sometimes multiscale modelling should be considered in a more complicated system, thus a space frame modelling, where atoms and bonds are modelled as nodes and straight springs, may be more effective in accurately predicting the results.[104]

MD based on the integration of Newton's motion equations is an effective method for probing into the mechanical properties and behaviour of 2D nanosheets. Firstly, a simulation cell containing hundreds to tens of thousands of atoms is relaxed at a preset temperature to reach an equilibrium state through an energy minimization process. Then, loading controlled by strain rate is applied to the nanosheet along different directions. In order to obtain Young's modulus, an atomic stress method[107–109] and an energy method[53] are usually used in MD. Since stress–strain curve can be obtained by MD calculations, corresponding fracture stress and fracture strain are typically defined at the peak point of the curve. Additionally, the simulation process combined with stress–strain curves can give access to the mechanical behaviour of 2D nanosheets. However, it is worth noting that the accuracy of atomistic simulation highly depends on the selected models and parameters such as interaction potential, boundary conditions, cutoff distance and step time. As a consequence, a validation is necessary prior to the effective simulations.

DFT is a computational quantum mechanical modelling method that have been widely used in this area. There are similar procedures of minimization and loading as that of MD, allowing for further determination of Young's modulus (or in-plane stiffness) and Poisson's ratio by strain energy method. For homogeneous and isotropic materials, elastic constants can be derived from strain energy of the elastic deformation in the harmonic range.[54,110,111] When at large strains, calculations based on nonlinear elastic theory are indispensable for describing anharmonic behaviour.[62,112,113] Since some 2DLMs (WTe_2,[114] phosphorene,[115] graphyne,[116] *etc.*) are mechanically anisotropic, a general model[115] has been further developed to calculate Young's modulus along different directions.

3. Mechanical properties and behaviour

Theoretically, the mechanical properties and behaviour of 2DLMs can be understood from the variation of strain energy during their deformation as shown in Fig. 6(a). There are two regions respectively named elastic region and plastic region

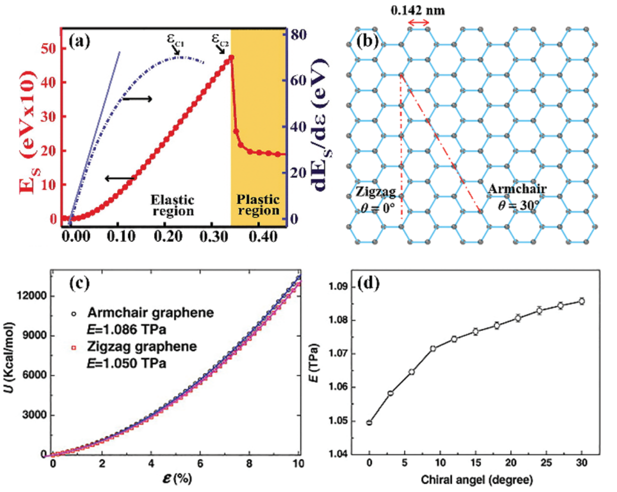

Fig. 6 (a) The variation of strain energy E_S of graphane with respect to strain ε and its derivative. (b) Chirality structure of graphene: zigzag direction for θ = 0°, and armchair direction for θ = 30°, where θ is the chiral angle. (c) U (strain energy)–ε (strain) curve of armchair and zigzag graphene sheets (GSs) (solid lines represent polynomial fitting). (d) Young's modulus of GSs for different chiral angles. Reprinted with permission from ref. 111. Copyright 2010 AIP Publishing. Reprinted with permission from ref. 53. Copyright 2010 Elsevier.

during deformation. In the elastic region, the strain energy monotonically increases without bonds breaking. According to the relationship between the derivative of strain energy and strain, the elastic region can be divided into harmonic region for linear relationship and anharmonic region for nonlinear relationship. Higher order terms should be considered for extracting elastic constants from the anharmonic region. When the applied strain reaches the plastic region, an irreversible structural change will occur and result in phase transitions or failure.[117] The critical strain corresponding to the peak of the derivative shown in Fig. 6(a) was reported to be related to the phonon instability.[111] Therefore, elastic instability and phonon instability are the two failure mechanisms of perfect 2DLMs. But some 2DLMs may exhibit ductile failure due to defects[73,118,119] or interfaces.[120] In this part, recent progress of both the elastic properties and failure mechanisms of different 2DLMs will be analyzed. The critical mechanical constants[4,53,54,61,62,72,74,76,81–85,87,89,92,93,103,108,109,111–113,116,117,119,120,122,125,126,128,132,134,135,141,142,144–146,148,152–173] have been summarized in Fig. 14.

3.1 Elastic properties

In 2DLMs, in-plane stiffness and Poisson's ratio play a critical role in the applications of flexible and stretchable nanodevices. Additionally, pretension is also an important parameter that should be considered in nanomechanical systems for determining deformation, resonant frequency and quality factor.[103] Since in-plane stiffness and Poisson's ratio are the intrinsic properties that are highly dependent on their crystal structures, chirality, bond types, bond strength and buckled structures are very critical in determining the elastic properties of 2DLMs. Instead, pretension of 2DLMs that can only be acquired by experimental methods is susceptible to external conditions such as preparation methods, characterization methods and the environments. In order to clearly show the structural and mechanical differences of 2DLMs, these materials are classified as planar structure (graphene), sp-hybridized structures (graphyne family), buckled structures (graphane, silicene and phosphorene), honeycomb structures (h-BN, TMDs and TMCs) and heterostructures (in-plane heterostructures and out-of-plane heterostructures), and their intrinsic elastic properties will be discussed in detail.

As Fig. 6(b) shows, graphene consists of in-plane hex rings where neighbour carbon atoms are separated by 0.142 nm.[121] The chirality of graphene can be characterized by chiral angle θ (zigzag for $\theta = 0°$, armchair for $\theta = 30°$). Generally, corresponding armchair and zigzag edges can also be found in other graphene-derived and graphene-like materials. Previous AFM-based indentation experiments have demonstrated that graphene is by far the strongest material with an in-plane stiffness of 250–360 N m^{-1} and a pretension of 0.05–0.8 N m^{-1}.[4,122] Assuming the effective thickness is 0.335 nm, the corresponding Young's modulus is 0.75–1.07 TPa. Such a strong Young's modulus should be attributed to the extremely strong sp^2 hybridization of C–C bonds and its high-quality of no defects. In addition, the elastic modulus obtained from experiments are in good agreement with that from MD[108,120,123] and DFT.[111] However, graphene grown by chemical methods is much weaker than pristine graphene due to the surface ripples.[50] This weaker property also exists in reduced graphene oxide (rGO) monolayers whose mean Young's modulus and pretension are ~0.25 TPa and ~4 nN, respectively.[87] Since graphene has a hexagonal structure with six-fold symmetry, its Young's modulus has been theoretically proved to be independent of the chirality as shown in Fig. 6(c) and (d). While the Poisson's ratio of graphene is around 0.16–0.17.

The structure of graphyne family (shown in Fig. 7(a)–(d)) can be formally viewed as resulting from the replacement of aromatic C–C bonds in graphene by acetylenic chains.[124,125] The mechanical properties of graphyne family have been confirmed to be greatly reduced compared to graphene by simulation calculations and theoretical analysis due to the introduction of sp-hybridized acetylenic bonds.[112,116,125–127] By MD simulations, the calculated 2D moduli of α- and γ-graphyne were 44 N m^{-1} and 174 N m^{-1} along zigzag direction, and 45 N m^{-1} and 182 N m^{-1} along armchair direction.[116] Besides, the Poisson's ratios of γ-graphyne and graphene were much smaller than that of α-graphyne. These results were thought to be closely related to their area densities (0.1159 $Å^{-2}$ for α-graphyne, 0.2902 $Å^{-2}$ for γ-graphyne, and 0.3818 $Å^{-2}$ for graphene), because lower area densities indicated less energy will

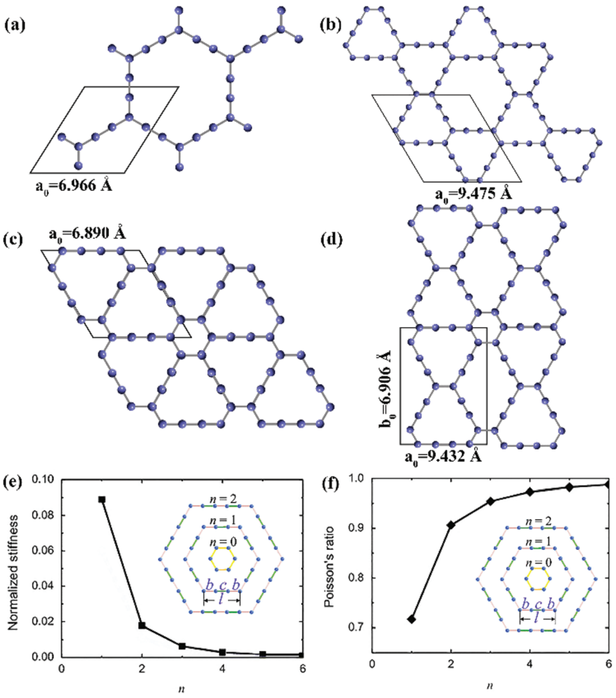

Fig. 7 Schematic of (a) α-, (b) β-, (c) γ-, and (d) 6,6,12-graphyne. Quadrangles indicate unit cells. (e), (f) In-plane stiffness (normalized by the corresponding values for graphene) and Poisson's ratio of α-graphyne with respect to the index number *n*. Inset in (e) and (f) is the schematic of extended α-graphyne. Reprinted with permission from ref. 125. Copyright 2016 Springer Nature.

be needed to stretch and rotate bonds. While average coordination number, in-plane atomic mass and electronic charge density were considered as the reasons for lower in-plane stiffness and higher Poisson's ratio of γ-graphyne compared to graphene through DFT calculations.[112] Thus, it is not difficult to understand that the Young's modulus of the graphyne family follows a certain order: $E_\alpha < E_\beta < E_{6,6,12} < E_\gamma$.[128] Moreover, it has been demonstrated that the in-stiffness of α-, β- and γ-graphyne decreased while the Poisson's ratio increased as the length of acetylenic chains increased (shown in Fig. 7(e) and (f)).[125–127] The degradation of in-plane stiffness was a result of the reduced effective bond density, while the enhancement of Poisson's ratio was due to the weakened bending resistance of acetylenic chains.

Graphane with similar honeycomb structure has been theoretically predicted by first-principles total energy calculations[129] and experimentally synthesized by exposing graphene to hydrogen plasma discharge.[35] As shown in Fig. 8(a), a chair-like buckled structure in graphane is formed due to the hydrogenation of carbon atoms on both sides of the plane. According to the theoretical results, the buckling distance between the alternating carbon atoms is 0.46 Å, and the bond length of C–C and C–H are 1.52 Å and 1.11 Å, respectively.[111,129] Consequently, the change of bonding type from sp^2 to sp^3 and the buckled structure softened the elastic properties of graphane with an in-plane stiffness of 243 N m^{-1}.[111] Besides, the Poisson's ratio of 0.07 was much smaller than that of graphene due to the reduced transverse contraction of the buckled structure.

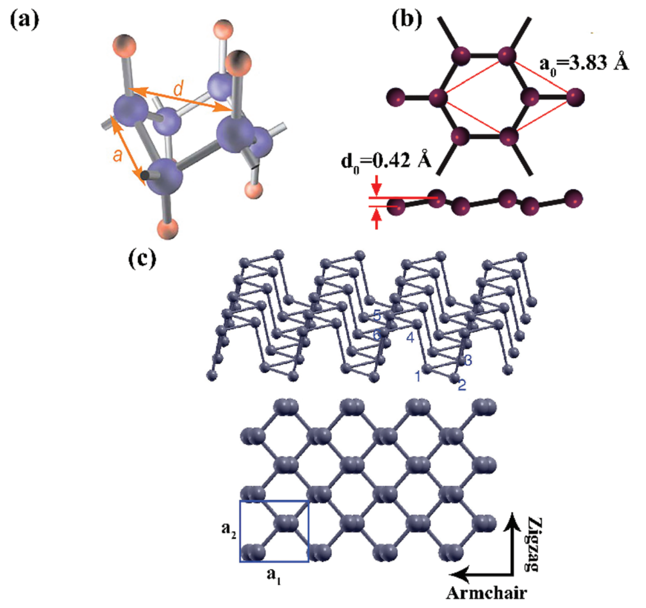

Fig. 8 (a) Structure of buckled graphane. (b) Top (top inset) and side (bottom inset) views of buckled silicene. The lattice constant a_0, buckling distance d_0 and Si–Si bond length are 3.83, 0.42 and 2.25 Å, respectively. (c) Perspective (top inset) and top (bottom inset) views of buckled phosphorene. Bond lengths: $d_{12} = d_{13}$ = 2.4244 Å, and d_{14} = 2.3827 Å. Bond angles: $\theta_{214} = \theta_{314}$ = 97.640°, and θ_{213} = 98.213°. The blue box represents the basic unit cell for phosphorene with two lattice constants of a_1 = 4.1319 Å and a_2 = 3.6616 Å. Reprinted with permission from ref. 35. Copyright 2009 The American Association for the Advancement of science. Reprinted with permission from ref. 134. Copyright 2014 Springer Nature.

Silicene is expected to have a buckled honeycomb structure (shown in Fig. 8(b)) arranged by Si atoms with an electronic dispersion resembling that of relativistic Dirac fermions.[54,130] Si–Si bond is longer than C–C bond, thus the structure of silicene has to pucker to form sp^3-like orbitals which can help stabilize the honeycomb structure. The results of MD[131] and DFT[54] calculations yielded an in-plane stiffness of 60.5–68.7 N m^{-1}, both indicating that silicene was much less stiff than graphene because the bonding between adjacent sp^3-like orbitals was much weaker than π bond in graphene. But the Poisson's ratio was found to be greater than that of graphene, which could be explained by longer Si–Si bond length and its low buckled structure.

Phosphorene has a highly puckered structure where each P atom is connected to three neighbouring P atoms as shown in Fig. 8(c). It is obvious that the armchair direction is perpendicular to the pucker and the zigzag direction is parallel to the pucker. According to the results from experiments and simulations,[83,115,132] phosphorene exhibited highly chirality-dependent mechanical properties where the Young's modulus in the zigzag direction was much larger than that in the armchair direction, even reaching 3.8 times at 0 K. The reason behind was that the tensile strain in armchair direction effectively flattened the pucker rather than extensively extending the P–P bond lengths and opening the bond angles.[115] When compared to other 2DLMs with similar honeycomb structures, such as graphene,[4] graphane,[111] WS_2,[84] MoS_2 [69] and h-BN,[133] the weaker P–P bond strength and compromised dihedral angles made the ideal Young's modulus of phosphorene (0.166 TPa in the zigzag direction and 0.044 TPa in the armchair direction) at 0 K much smaller. Besides, the pretension of few-layer black phosphorus was determined experimentally to be in the range of 0.05–0.44 N m^{-1},[83,93] and thicker nanosheets had smaller values because of their stronger structural stiffness. Interestingly, phosphorene has a negative Poisson's ratio of −0.027 in the out-of-plane direction when the strain is applied in the zigzag direction due to the coupling hinge mechanism where the hinge θ_{546} and θ_{214} in Fig. 8(c) are opened and closed, respectively.[134] This kind of 2D auxetic material will be very desirable in the nanoscale electromechanical devices with special functions.

h-BN is a promising dielectric with a large band gap of ~5.5 eV.[133] Alternating boron and nitrogen atoms bound by strong covalent bonds arrange in a honeycomb structure as shown in Fig. 9(a). Due to the better maintained hexagonal structure and preservation of sp^2-hybridized state, the theoretical Young's modulus of pristine h-BN was in the range of 716–977 GPa,[135] which was very close to pristine graphene mentioned earlier. Further AFM-based indentation on 1–2 nm thick h-BN indicated that its in-plane stiffness was 220–510 N m^{-1}.[133] This may be attributed to the layer distribution of stacking faults in the CVD grown films or the error during the experi-

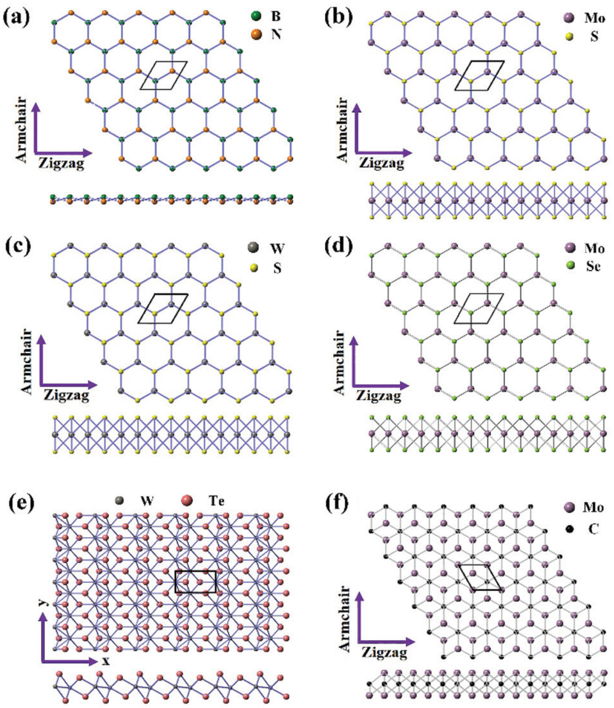

Fig. 9 Top and side views of the atomic structure of monolayer (a) h-BN, (b) MoS_2, (c) WS_2, (d) $MoSe_2$, (e) T_d-WTe_2, and (f) Mo_2C. Black rhombus or rectangular represents a unit cell. Lattice constants: (a) $a = b = 2.498$ Å, $c = 15$ Å, $\alpha = \beta = 90°$ and $\gamma = 120°$, (b) $a = b = 3.15$ Å, $c = 12.3$ Å, $\alpha = \beta = 90°$ and $\gamma = 120°$, (c) $a = b = 3.18$ Å, $c = 12.5$ Å, $\alpha = \beta = 90°$ and $\gamma = 120°$, (d) $a = b = 3.288$ Å, $c = 12.9$ Å, $\alpha = \beta = 90°$ and $\gamma = 120°$. (e) The x direction is parallel to the W–W dimer direction, while the y direction is perpendicular to the W–W dimer direction. Lattice constants: $a = 6.282$ Å, $b = 3.496$ Å, $c = 14.07$ Å, $\alpha = \beta = \gamma = 90°$. (f) Lattice constants: $a = b = 2.994$ Å, $c = 4.722$ Å, $\alpha = \beta = 90°$ and $\gamma = 120°$.

mental processes. While the corresponding Poisson's ratio of h-BN (0.21–0.41[136]) was a little larger than that of graphene.

TMDs and TMCs with similar sandwich structures consisting of three atomic layers (shown in Fig. 9(b)–(f)) have been proven to possess great potential in many practical applications.[44,137–140] Previous calculations[62,117,141] have demonstrated that the Young's modulus of MoS_2 is about one fifth of the Young's modulus of graphene, but DFT calculations trend to underestimate the values when compared to the results from experiments.[81,84,85,142] Assuming an effective monolayer thickness of 0.65 nm, the Young's moduli of single-layer and bilayer MoS_2 were determined to be 270 ± 100 GPa and 200 ± 60 GPa respectively, while the pretension of single-layer MoS_2 was in the range of 0.02 to 0.1 N m^{-1}.[142] Besides, the Young's modulus and pretension of MoS_2 with layers of 5–25 were measured to be 0.21–0.37 TPa and 0.03–0.23 N m^{-1}, respectively.[85] Both single layer and few layers MoS_2 behaved stiffer than bulk MoS_2 (0.24 TPa (ref. 143)), which was attributed to the lower stacking faults in nanosheets. Due to the similar lattice constants of WS_2 and MoS_2, the Young's modulus and pretension of WS_2 are very close to that of MoS_2.[84] However, the average elastic modulus (177.2 GPa (ref. 74)) of single-layer and bilayer $MoSe_2$ measured by *in situ* tensile testing was a little lower than MoS_2 and WS_2, which may be the result of different methods of sample fabrication and characterization. Unlike isotropic 2H-MoS_2, 2H-WS_2 and 2H-$MoSe_2$ discussed above, T_d-WTe_2 (shown in Fig. 9(c)) is a typical anisotropic 2D material whose symmetry is broken by the dimerization of the W atoms along the x direction. The direction-dependent in-plane stiffness acquired by DFT calculations[144] were 4.45 eV Å^{-2} along x direction and 6.56 eV Å^{-2} along y direction respectively, while the corresponding Poisson's ratio were 0.26 and 0.38 respectively. Though there are many researches exploring the mechanical properties of TMDs, works on the mechanical properties of TMCs relatively lack. Recently, DFT calculations indicated that the Poisson's ratio of Mo_2C along armchair and zigzag directions were both ~ -0.15, but the negative Poisson's ratio was valid only at strain levels below the half of the ultimate strain.[144]

2D heterostructures can be defined as in-plane heterostructures linked by covalent bonds in the same layer and out-of-plane heterostructures linked by weak van der Waals interaction between vertical layers. Both of them exhibit a compromised Young's modulus.[84,120,145,146] Research[120] on the mechanical properties of in-plane graphene-BN heterostructure revealed that Young's modulus along both armchair and zigzag directions decreased with increasing concentration of BN. Additionally, Liu *et al.*[84] qualitatively probed into the interaction of bilayer vertical hetero- or homostructures (shown in Fig. 10(a) and (b)). Since the bottom layer was firmly clamped onto the substrate, the measured modulus of bilayer structures was mainly dependent on the contribution of the top layer which was possible to slide during the indentation tests. Further analysis indicated that interaction factor α could be employed as a parameter to compare the interlayer coupling in different bilayer hetero- or homostructures, thus determining the interaction coefficients of MoS_2/MoS_2, MoS_2/WS_2, MoS_2/graphene, and graphene/graphene to be 0.75, 0.80, 0.69 and 1.0, respectively. The similar values of interaction coefficient of MoS_2/MoS_2 and MoS_2/WS_2 suggested that the interaction between MoS_2 and WS_2 was comparable to that in bilayer MoS_2. While there was a relatively strong interaction between graphene homolayers. Besides, the mechanical pro-

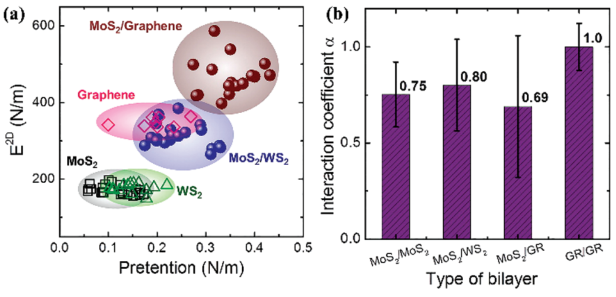

Fig. 10 (a) Experimental data of 2D modulus and pretension for various 2D layers and heterostructures. (b) Interaction coefficients for different types of bilayers. Reprinted with permission from ref. 84. Copyright 2014 American Chemical Society.

perties of a kind of sandwich structure heterostructures have been theoretically studied, including graphene/MoS_2/graphene[145] and graphene/silicene/graphene.[146] In these studies, an empirical formula has been used to predict the Young's modulus.[145,146] The predicted results were 511.76 GPa for graphene/MoS_2/graphene and 620 GPa for graphene/silicene/graphene, which were basically consistent with the results from MD calculations.

3.2 Failure mechanisms

A failure will occur when 2DLMs are strained to their limits. To avoid the failure of nanodevices based on 2DLMs, the applied stress and strain should be strictly controlled under the limit values. Herein, three failure mechanisms related to 2DLMs are discussed and summarized as shown in Table 3.

3.2.1 Brittle failure. In essence, 2DLMs free of defects trend to be brittle failure[71,73,74] like $MoSe_2$ (shown in Fig. 11). According to the fracture theory of Griffith,[147] the upper theoretical limit of breaking strength of defect-free brittle materials is ∼1/9 of corresponding Young's modulus. Due to the inevitable defects and flaws in 3D materials, it's difficult to verify this theory *via* experiments on traditional materials. Therefore, 2DLMs are the most likely target for direct and repeatable measurements of the intrinsic strength. The breaking strengths obtained by AFM-based indentations on single-layer graphene[4] and MoS_2 [62,142] were in excellent agreement with the predicted values, further demonstrating that brittle failure may be the inherent behaviour of 2DLMs at room temperature. But the strengths of different 2DLMs exhibit huge differences because of different structures and bond strengths. With the increase of acetylenic chains introduced in γ-graphyne, 6, 6, 12-graphyne, β-graphyne and α-graphyne, their corresponding strengths were significantly reduced in turn.[128] While the failure stress and strain of γ-graphyne heavily depended on the direction of the applied strain and the alignment with acetylenic chains.[148] The buckled structures in graphane,[111] silicene[131] and phosphorene[115] also lead to a greatly weakened strength compared to graphene. For vertical heterostructures, the failure is defined as the failure of any layer. Thus, their strength is expected to be limited by the layer with lower failure strain, which is the case with graphene/silicene/graphene heterostructure.[146]

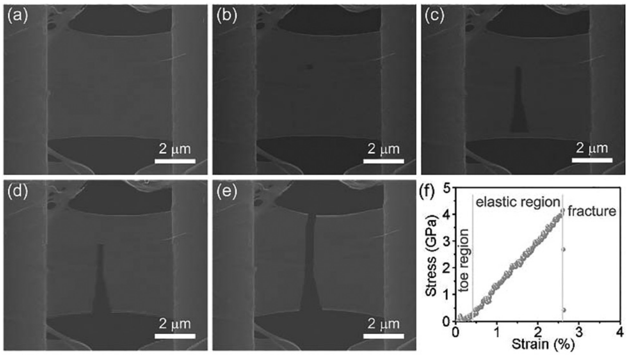

Fig. 11 (a) SEM image of $MoSe_2$ before tensile testing. (b)–(e) SEM images showing the fracture process. (f) Measured stress–strain curve. Reprinted with permission from ref. 74. Copyright 2016 John Wiley and Sons.

Though the intrinsic strength of these perfect 2DLMs discussed above is critical in determining the life and performance of nanodevices, it's of more practical significance to study their fracture toughness. Zhang *et al.*[70] operated an *in situ* tensile testing of suspended bilayer graphene, revealing that the failure of pre-cracked graphene was due to the brittle fracture. Theoretical stress intensity factor and critical strain energy release rate were experimentally determined to be $4.0 \pm 0.6\,\mathrm{MPa}\sqrt{m}$ and $15.9\ \mathrm{J\ m^{-2}}$, respectively. While the critical stress intensity factor of multilayer graphene and h-BN was measured to be 12.0 ± 3.9 and $5.5 \pm 0.7\,\mathrm{MPa}\sqrt{m}$ respectively by Wei *et al.*[71] The difference between Zhang's results and Wei's results should be ascribed to the different fracture mechanisms that exist in bilayer graphene and multilayer graphene. Bilayer graphene fractured along a smooth edge while multilayer graphene and h-BN exhibited rough fracture edges caused by crack meandering and branching which could increase the energy required for a crack to propagate. Recently, MD calculations[149] revealed that the failure stress and strain for armchair and zigzag directions trended to decrease with the increase of pre-crack size in graphene. The critical stress intensity factors of pre-cracked graphene at 0 K and 300 K were calculated to be $8.4 \pm 1.27\ \mathrm{MPa}\sqrt{m}$ and $7.4 \pm 1.52\,\mathrm{MPa}\sqrt{m}$, respectively. However, the fracture tough-

Table 3 Failure mechanisms of 2DLMs

Failure mechanism	Characteristic	Conditions	Ref
Brittle failure	Failing by propagation of cracks	Materials free of defects	71, 73 and 74
Ductile failure	Plastic deformation by generation of reformed bonds or dislocations at crack-tips	Highly defected graphene	118 and 119
		Highly vacancy-defected MoS_2	73
		In-plane heterostructure graphene-BN (loading along armchair direction)	120
Phonon instability	Imaginary frequencies appearing before elastic instability	Graphene under equibiaxial strain	151
		Graphane under uniform expansion	111
		Silicene under uniform expansion	54
		MoS_2 subjected to biaxial strain or uniaxial strain along the armchair direction	141

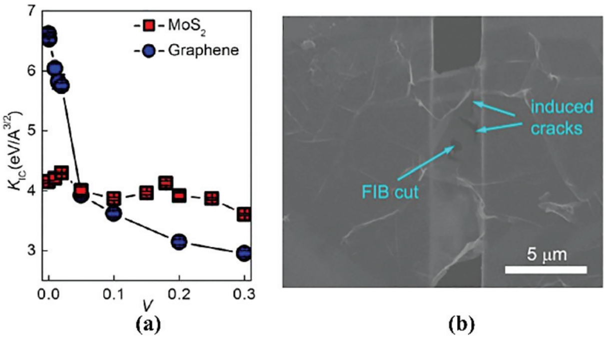

Fig. 12 (a) Comparison of fracture toughness as a function of vacancy density for MoS_2 and graphene. (b) Catastrophic fracture of $MoSe_2$ during FIB cutting. Reprinted with permission from ref. 73. Copyright 2016 American Chemical Society. Reprinted with permission from ref. 74. Copyright 2016 John Wiley and Sons.

ness of graphene obtained above is relatively low compared to conventional bulk materials,[75] which will induce reliability issues in their further applications as nanodevices. To improve the fracture toughness of graphene, high fracture toughness of ~39 J m^{-2} was realized by chemical functionalization.[75] MD simulations indicated that the interactions among functionalized atoms in constituent layers and distinct fracture pathways in individual layer resulted in the huge enhancement of fracture toughness. As for TMDs, it was found that the crack propagation of CVD-grown monolayer MoS_2 preferentially occurred along the zigzag direction during brittle fracture,[73] differing from graphene for fracturing along both armchair and zigzag directions.[150] With the increase of vacancy density, a gentle reduction of fracture toughness of MoS_2 was observed while graphene has a more dramatic change in fracture toughness (shown in Fig. 12(a)). Though Yang *et al.*[74] have attempted to measure the fracture toughness of $MoSe_2$, catastrophic fracture (shown in Fig. 12(b)) is unavoidable during the introduction of pre-crack by focus ion beam (FIB). Therefore, how to fabricate the samples of 2DLMs with great brittleness for fracture toughness measurement is a big challenge for future exploration of their mechanical properties. The fracture toughness mentioned above is summarized in Table 4.

3.2.2 **Ductile failure.** Ductile materials are able to undergo larger plastic deformation by generation of reformed bonds or dislocations at crack-tips. Though pure graphene fractures in a brittle manner, it has been demonstrated by MD calculations that the transformation from brittle failure to ductile failure will occur in the highly defective graphene.[118] This behaviour can be explained by crack trapping of sp–sp^2 (for highly vacancy-defected graphene) or sp–sp^2–sp^3 (for highly Stone–Wales-defected graphene) rings and crack-tip blunting. However, the similar brittle-to-ductile transition was observed in the highly vacancy-defected graphene (shown in Fig. 13(a) and (b)) with the vacancy concentrations of 8%–12%,[119] while the vacancy-induced crystalline-to-amorphous transition of graphene was thought to be the key factor accounting for the ductile behaviour. In addition, by *in situ* observation of fracture process of monolayer MoS_2, it was clearly clarified that the increasing vacancy density shifted the fracture mechanisms from brittle to ductile by the migration of vacancies in the strain field into networks.[73] Except defects, the interface of the in-plane heterostructure graphene-BN also gave rise to the ductile behaviour along armchair direction which was absent in pure graphene and h-BN.[120] The different behaviour along armchair (ductile failure) and zigzag (brittle failure) directions was ascribed to the relation between the interface and the mechanical loading direction.

3.2.3 **Phonon instability.** Phonon instability will occur when imaginary frequencies appear before elastic instability, indicating an instability of 2DLMs under such strain condition. This novel soft-mode phenomenon has been reported in graphene,[151] graphane,[111] silicene,[54] and MoS_2.[141]

Even though previous phonon calculations have demonstrated that elastic instability is the failure mechanism of graphene under uniaxial strain in armchair and zigzag directions,[152] further summarizations[151] of all possible failure mechanisms of pure graphene at 0 K (shown in Fig. 13(c)) indicated that the strength of graphene was limited by the phonon instability under equibiaxial strain. However, the calculated failure strain of 0.151 caused by the K_1 mode was much smaller than the experimental results of 0.225,[4] which may be attributed to the differences in temperature and the reaction between tip and graphene. Phonon instability has also been proven to be the failure mechanism in graphane and silicene under uniform expansion, yielding a failure strain of ~0.23[111] and ~0.18,[54] respectively. Besides, DFT calculations have found that the tensile strength was dictated by phonon instability when MoS_2 was subjected to biaxial strain (shown in Fig. 13(d)) or uniaxial strain along the armchair direction (shown in Fig. 13(e)), while limited by elastic instability for the

Table 4 Fracture toughness of 2DLMs

Materials	Synthetic method	Layers	Fracture toughness		Ref.
			K_C (MPa$\sqrt{m}$)	G_C (J m^{-2})	
Graphene	—	1	6.6 eV Å^{-1}/$\sqrt{Å}$	2.3 eV Å^{-1}	73
Graphene	CVD	2	4.0 ± 0.6	15.9	70
Graphene	Arc-discharge	6–20	12.0 ± 3.9	—	71
h-BN	Induction heating	10–12	5.5 ± 0.7	—	71
MoS_2	CVD	1	4.2 eV Å^{-1}/$\sqrt{Å}$	2.5 eV Å^{-1}	73
GO	Chemical functionalization	~21	—	34–39	75
GO	Chemical functionalization	~30	—	81	75

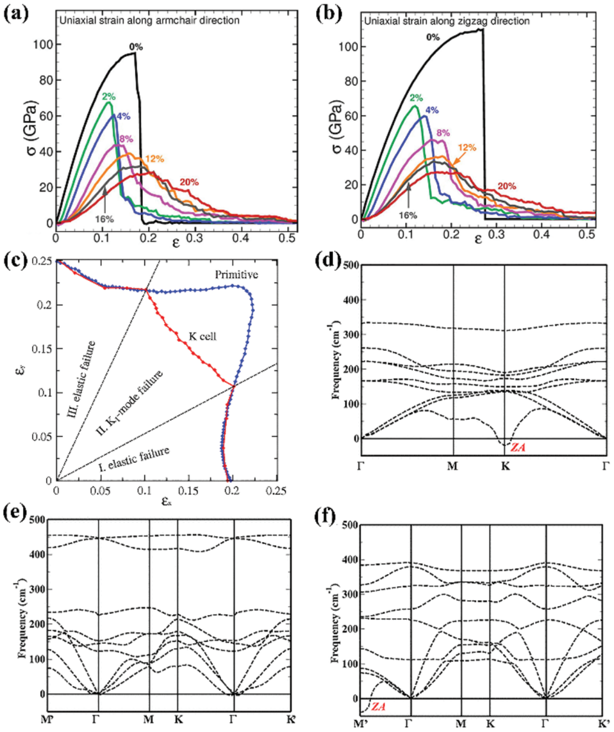

Fig. 13 Stress–strain response of defective single-layer graphene (vacancy concentrations are indicated in the figure) subjected to uniaxial tensile strain along armchair (a) and zigzag (b) directions. (c) The maximum stable strain for the primitive unit cell (blue curve) and the *K* cell (red curve) as a function of all possible linear combinations of zigzag and armchair uniaxial tensile strains. Calculated phonon dispersion for single layer MoS_2 at (d) biaxial tension with ε = 0.195, (e) uniaxial tension along zigzag direction with ε = 0.36 and (f) uniaxial tension along armchair direction with ε = 0.28. Reprinted with permission from ref. 119. Copyright 2013 AIP Publishing. Reprinted with permission from ref. 151. Copyright 2010 American Physical Society. Reprinted with permission from ref. 141. Copyright 2012 American Physical Society.

zigzag direction (shown in Fig. 13(f)).[141] The predicted ideal strengths are in great agreement with the experimental results,[85,142] further verifying the validity of the calculation results. But this phonon instability present in MoS_2 is due to the out-of-plane atomic relaxation upon in-plane strain which is different from that of the truly 2D graphene.

4. Influence factors on the mechanical properties

During the process of growth, transfer, design, fabrication and usage, the factors of great influence on intrinsic mechanical properties of perfect 2DLMs should be taken into consideration for practical applications. In turn, the mechanisms of these factors provide effective means for accurately tailoring their mechanical properties.

4.1 Defects

Noted that the difference of mechanical properties of 2DLMs fabricated by different methods could be attributed to the influence of produced defects, and thus it is possible to tailor the mechanical properties during their fabrications.

4.1.1 Point defects—vacancies and Stone–Wales (SW) defects. Among these point defects observed in 2DLMs (shown in Fig. 15), the significant effects of vacancy and SW defects on the mechanical properties and behaviour of 2DLMs have been

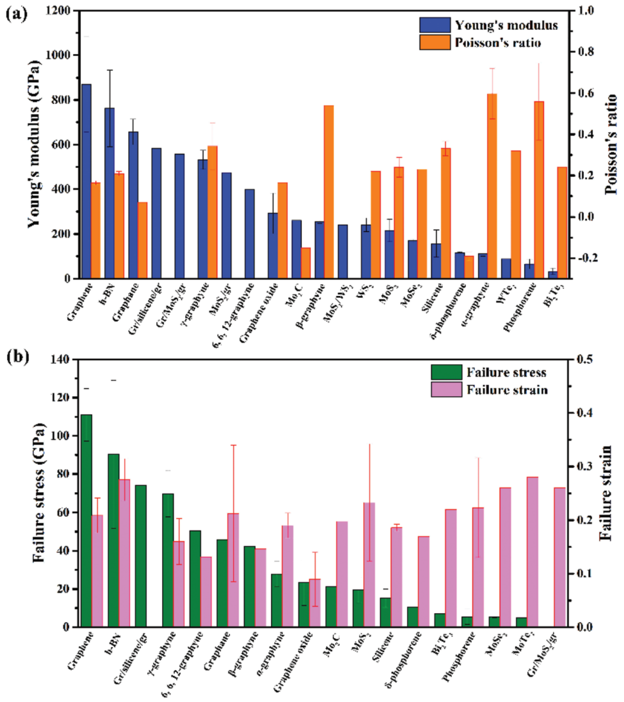

Fig. 14 (a) Young's modulus and Poisson's ratio with standard deviations of 2DLMs. (b) Failure stress and strain with standard deviations of 2DLMs.

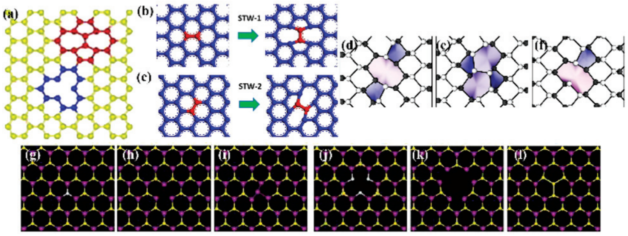

Fig. 15 Point defects in 2DLMs. (a)–(c) Vacancy and SW defects in graphene. Red C–C bond rotates by 90° to the SW-1 defect (b) and red C–C bond rotates by 90° to the SW-2 defect (c). (d)–(f) Vacancy and SW defects in phosphorene, including divacancy (d), SW (e) and monovacancy (f). (g)–(l) Six types of point defects in MoS_2 observed in experiments. From left to right: monosulfur vacancy (g), disulfur vacancy (h), antisite defects where a Mo atom substituting a S_2 column (i), vacancy complex of Mo and nearby three sulfur (j), vacancy complex of Mo nearby three disulfur pairs (k) and antisite defects where a S_2 column substituting a Mo atom (l). Reprinted with permission from ref. 123. Copyright 2011 AIP Publishing. Reprinted with permission from ref. 174. Copyright 2014 Elsevier. Reprinted with permission from ref. 175. Copyright 2014 American Chemical Society. Reprinted with permission from ref. 176. Copyright 2013 American Chemical Society.

systematically investigated by MD simulations or experiments. Vacancies and SW defects controlled by concentration and arrangement can significantly reduce the strength of 2DLMs due to the stress concentration around defects. MD simulations revealed that the strength of phosphorene,[51] graphene[118,123] and h-BN[135] decreased almost linearly with defect concentration. Typically, a small concentration of vacancy defects can lead to a significant decrease of strength[51,118,119,122] owing to the crack nucleation sites provided by vacancies. Moreover, the fracture stress decreased with the increasing of tilt angle α between the direction of stretching and the direction of linearly arranged monovacancies due to the reduction of effective cross-sectional area.[51] However, unexpectedly to these simulation results, AFM indentation on mechanically exfoliated graphene revealed that the in-plane stiffness even increased during the initial rise of vacancy concentration (shown in Fig. 16(b)) due to the competing mechanisms between the conventional softening effect of vacancies and the strengthening effect of defects by decreasing the mean free path of flexural phonons (shown in Fig. 16(a)). This gap between simulations and experiments arose from the fact that the former did not consider the influence of defects to the thermodynamic effect of graphene membrane. The Young's modulus[123] and strength[118,167,174] of 2DLMs were also degraded by the presence of SW defects. But the variation of Young's modulus with SW defect concentration in graphene was more stable than that of vacancy because SW defects containing two heptagons and two pentagons (shown in Fig. 15(b) and (c)) preserved the sp^2 bonding structure.[123] Further study[174] demonstrated that the strength of single-SW defective graphene was strongly related to the chirality. The STW-1 graphene had a much larger strength in the zigzag direction than armchair direction, which was just the opposite of STW-2 graphene. In addition, when the tilt angle increased (shown in Fig. 16(c) and (d)), the strength of graphene with multiple linear SW defects decreased due to the reduction of cross-sectional area. It was worth noting that the strength could be even bigger than that of single STW defective graphene when the tilt angle was smaller than 25°, indicating that the strength of graphene could be adjusted by defects arrangements in a relatively large range.

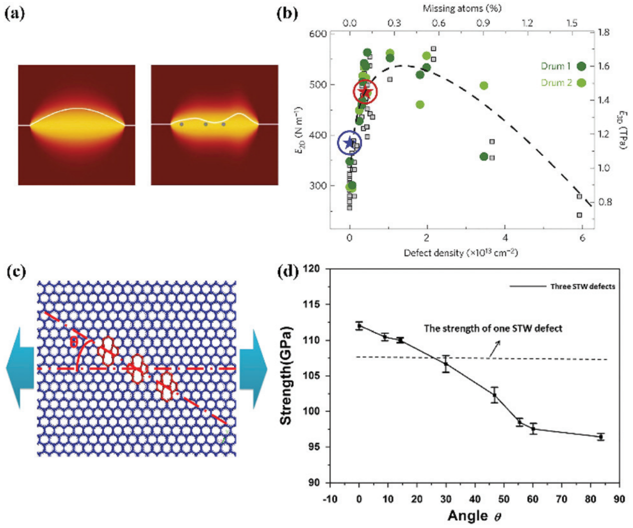

Fig. 16 (a, b) Experimentally determined 2D Young's modulus (E^{2D}) of graphene with various defect densities. Left picture in (a) depicts the thermal fluctuation of a suspended graphene membrane, while right picture indicates that long-wavelength fluctuations are quenched in the presence of defects. (c, d) Strength of defective graphene with SW defects. The strength represented by the dashed line in (d) is 107.60 GPa, corresponding to the strength of graphene with a single SW-1 defect stretched along the zigzag direction. Reprinted with permission from ref. 122. Copyright 2014 Springer Nature. Reprinted with permission from ref. 174. Copyright 2014 Elsevier.

Meanwhile, the mechanical behaviour of 2DLMs can also be influenced by vacancies and SW defects. The failure behaviour of highly defective graphene with vacancies and SW defects can be transformed from brittle rupture to ductile fracture due to the combined results of crack trapping, crack-tip blunting and crystalline-to-amorphous transition.[118,119] In addition, *in situ* observation of the fracture of monolayer MoS$_2$ with high S vacancies confirmed that the line defects formed by the aggregation of S vacancies could help to guide and deflect the crack in propagation, thus inducing the brittle-to-ductile transformation.[73] Besides, by MD simulations, the nucleation and evolution of a fracture induced by vacancies and SW defects in h-BN were even directional.[167]

4.1.2 Line defects—dislocations and grain boundaries. Dislocation is the basic unit cell of grain boundaries that control the deformation of 2DLMs. Due to the planar structure of 2DLMs, an equivalent of an edge dislocation with the Burgers vector constrained to lie in the 2D plane is imagined to describe the dislocations in 2DLMs.[52,177] That means only edge dislocations are possible to be observed in 2DLMs, thus dislocations and grain boundaries in these materials are line defects. As Fig. 17 depicted, various dislocations and grain boundaries in different 2DLMs are listed for better understanding of their effects on the mechanical properties and behaviour. There are three kinds of basic dislocations consisting of heptagon-pentagon pairs and two kinds of grain boundaries respectively corresponding to the armchair (LAGB I) and zigzag (LAGB II) orientations in graphene (shown in Fig. 17(a)). The theoretical limit of misorientation angle θ ($\theta = \theta_1 + \theta_2$) are 21.8° and 32.2° for LAGB I and LAGB II, respectively. As for MS$_2$ (M = Mo or W), the prediction of dislocations uncovered three kinds of possible basic edge forms (shown in Fig. 17(b)), including a pentagon-heptagon with M–M central pair for Burgers vector (1, 0), a square-octagon for Burgers vector (1, 1) and a pentagon-heptagon with S–S central pair for Burgers vector (0, 1). However, DFT calculations indicated that an isolate square-octagon pair was unstable and split into a pair of pentagon-heptagon ($(1, 1) \rightarrow (1, 0) + (0, 1)$).[178] Therefore, the grain boundaries formed by pentagon-heptagon pairs can be mirror-symmetric armchair A-GB with same polarity (either M-rich (blue) or S-rich (yellow)) in the opposite edges or asymmetric zigzag Z-GB with different polarities in the opposite edges as shown in Fig. 17(c). But it should be

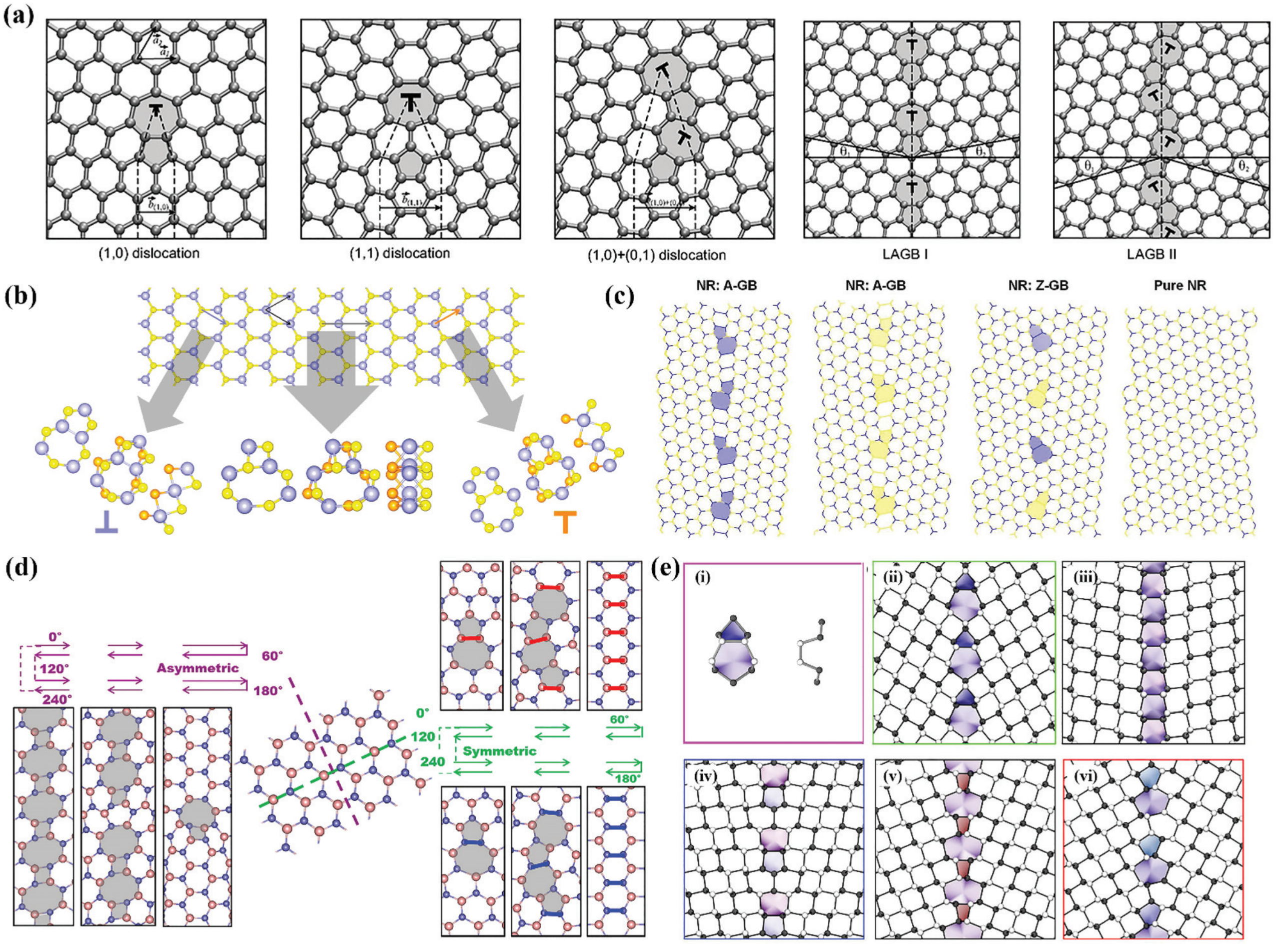

Fig. 17 (a) Atomic structures of (1, 0), (1, 1) and (1,0) + (0,1) dislocations as well as the θ = 21.8° (LAGB I) and the θ = 32.2° (LAGB II) symmetric large-angle grain boundaries in graphene. (b) Basic edge dislocations formed by removal of shaded atoms from the MS_2 (M = Mo or W) lattice. Each atomic structure is shown in front, isometric, and side (along the layer) views, with atoms colored blue (metal, M), yellow (front/top layer sulfur, S) and orange (back/bottom layer sulfur, S′). (c) Atomic structures of grain boundaries for mirror-symmetric armchair A-GB and asymmetric zigzag Z-GB in MS_2 (M = Mo or W). (d) Ground state structures of grain boundaries as a function of tilt angle in h-BN. (e) Top and side view (i) of the core structure of the primary dislocation with a Burgers vector (0, 1) and structure of grain boundaries at various misorientation angles in phosphorene (26.8° for (ii), 71.1° for (iii), 110° for (iv), 130° for (v) and 149° for (vi)). Reprinted with permission from ref. 177. Copyright 2010 American Physical Society. Reprinted with permission from ref. 178. Copyright 2013 American Chemical Society. Reprinted with permission from ref. 179. Copyright 2012 American Chemical Society. Reprinted with permission from ref. 175. Copyright 2014 American Chemical Society.

noted that a rich variety of grain boundaries of MoS_2 were experimentally observed with the predicted pentagon–heptagon pairs or distinct 4-fold ring chains.[176] One of the reasons why the basic dislocations of graphene and MS_2 (M = Mo or W) are different is that the latter is composed of the alternating arrangements of heterogeneous elements, and this is also the case of h-BN. Consequently, there are three types of basic dislocations composed of a pentagon–heptagon ring or a square-octagon ring similar to that in MS_2 (M = Mo or W), while the grain boundaries varies with the tilt angles which gives rise to the symmetric boundaries constituted by pentagon–heptagon pairs and asymmetric boundaries constituted by square-octagon pairs (shown in Fig. 17(d)). Fig. 17(e) shows the primary dislocation with a burgers vector (0, 1) and various grain boundaries corresponding to different misorientation angles in highly buckled phosphorene.

It is natural to believe that grain boundaries can reduce the mechanical properties of 2DLMs according to continuum mechanics theory. This weakening effect has been confirmed in graphene[180,181] and MoS_2.[182] But this point is proved to be unreliable to a certain extent by simulations[107] and experiments.[155] By MD and DFT calculations, it was suggested that the failure stress and strain would increase when the grain boundary angle increased.[107] This was ascribed to the fact that graphene with higher grain boundary angle had a bond length closer to that of the pristine graphene. However, the upper bound of in-plane breaking stress of graphene determined by AFM indentations[50] was lower than the theoretically predicted values,[107] which could be understood by the combined weakening effects of voids near boundary and the shear of boundaries under indentations. While in another study, the difference between the theoretical predictions and AFM indentation values was attributed to the fabrication methods of samples.[155] As a result, a new method for sample fabrication was developed by using ammonium persulfate for copper etching and polydimethylsiloxane for dry transfer. It was interesting to note that the grain boundary angle had no obvious effect on the strength of graphene in this study. This arose from the energy-minimizing structure of random asymmetric grain boundaries that could result in a smaller misfit "pre-strain" of the critical bonds in boundaries. On the other hand, it was indicated that the combination of the defect densities and the detailed arrangements of grain boundaries deeply affected the mechanical properties since the strength of grain boundaries could either increase for evenly spaced pentagon–heptagon defects or decrease for other cases.[180]

4.1.3 Crystal defect—functionalization. The effect of functionalization of 2DLMs must be considered for two reasons for nanodevices design. Firstly, wet chemical method[183,184] is usually utilized for the synthesis of large quantities of 2DLMs, which will introduce different functional groups. Secondly, sometimes several functional groups will be deliberately introduced to pure 2DLMs for performance optimization or specific functions development.[185,186] Since functionalization affects the mechanical properties by significantly changing the local crystal structures, the types, location, distribution and coverage of functional groups are of great importance in determining the mechanical properties.

For graphene, functionalization can be considered as the introduction of sp^3 bonds, thus resulting in the rise of carbon atoms with functional groups from the original plane. By MD and MM simulations,[53] the Young's modulus of graphene was reported to decrease linearly with the increasing coverage of hydroxyl groups because off-plane sp^3 bond was much easier to be bent and broke the local bond. Besides, functional group with higher binding energy had a more adverse effect on the Young's modulus, accounting for the reduction degree of graphene with carboxyl groups was bigger than that of graphene with propyl and methyl hydroperoxide groups. On the contrary, molecular weights of functional groups may have no obvious effect on the Young's modulus of graphene. The failure stress and strain trend to have a stronger sensitivity to functionalization than Young's modulus.[108,109] For example, functionalization of even one H atom in graphene can lead to a relative different drop in Young's modulus, failure stress and strain by 0.1%, 13% and 30%, respectively.[108] This can be understood from two aspects: (1) Young's modulus is a measure of average deformation of the whole system in the small strain regime while failure stress and strain are limited by the breakage of the weakest bonds; (2) sp^3 hybridized bonds are weaker than sp^2 hybridized bonds and will result in local stress concentration. Moreover, the location and distribution of introduced groups could also influence the strength of graphene.[109] Results showed that surface functionalization had a stronger effect than edge functionalization because edge functionalization only terminated the dangling bonds of graphene edges without the formation of sp^3 bonds. For different distributions, methyl groups arranged in line perpendicular to the tension direction led to a greater drop of failure stress and strain than that parallel to the tension direction. If the sp^3 bonds are viewed as weaker phase in graphene, it is not difficult to understand that the strong sp^2 bond network will be destroyed to the largest extent when the sp^3 bonds are arranged in line perpendicular to the tension direction. Even though the introduction of sp^3 bonds will degrade the mechanical properties of graphene, a relative small number of sp^3 bonds between bilayer graphene can achieve optimal load transfer rate and stability.[156]

Graphene oxides (GO) (shown in Fig. 18(a)) can be considered as graphene functionalized by oxygen-containing groups, such as hydroxyl (–OH) and epoxy (–O–) groups on the basal plane and carboxyl groups on the edge.[34,187] The functionalization of oxygen-containing groups breaking the sp^2 bond network is the reason for the weaker mechanical properties[103,160,161] than graphene. DFT calculations of the Young's modulus and strength of single-layer GO revealed that the increasing coverage of groups could further weaken its mechanical properties because of the breakage of sp^2 bond network.[161] But OH/O ratio had little effect on the mechanical properties of GO when the coverage maintained constant, indicating the coverage instead of the types of functional groups was the main factor in reducing the mechanical properties of GO. The weakening effect of coverage was further confirmed by AFM indentations where the obtained Young's moduli of monolayer GO with ~20% functionalization and ~40% functionalization were 269 ± 21 N m^{-1} (ref. 160) and 145.3 ± 16.4 N m^{-1},[103] respectively. Besides, the active oxygen-containing groups attached on GO makes it possible to synthesize composite materials with enhanced mechanical properties.[34] Due to different fracture mechanisms among monolayer GO, GO nanosheets and GO papers, the failure behaviour transforms from interlayer fracture for GO papers (or bulk GO) to absolute intraplanar fracture for monolayer GO,[72] accounting for the orders of magnitude discrepancy in strength (24.7 GPa

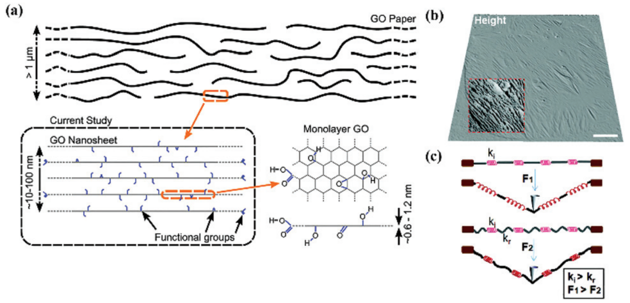

Fig. 18 (a) Schematic of the hierarchical units forming the basis of GO materials. (b) AFM height tapping mode image of graphene. The region in the red box is enlarged in the *z* direction. (c) Model illustrating a flat and a rippled graphene cross section. The springs have a spring constant k_i representing graphene's intrinsic elastic modulus. While flattening ripples have a much smaller spring constant k_r. Reprinted with permission from ref. 72. Copyright 2015 American Chemical Society. Reprinted with permission from ref. 50. Copyright 2011 American Chemical Society.

for monolayer GO,[160] 12 GPa for GO nanosheets[72] and ~100 MPa for GO papers[34,188]).

4.1.4 Structure defect—ripples. The ultralow bending stiffness of single- or few-layer 2DLMs is a cause of the spontaneous out-of-plane ripples (shown in Fig. 18(b)) during growth and transfer processes. Suspended graphene could exhibit intrinsic ripples with a height of up to 1 nm,[188] and this spontaneous effect has also been observed in MoS_2 [189] and h-BN.[190] The softening effect of these ripples could be understood from the models of a rippled membrane and a flat membrane with negligible bending stiffness as shown in Fig. 18(b). Thus, less force will be required to flatten the rippled membrane than to stretch the flat membrane, perfectly accounting for the softened Young's modulus of CVD grown graphene with sizable ripples.[50]

4.2 Others

Other researches have demonstrated that strain rate and substrate roughness have great influence on the mechanical properties and behaviour. While for material like phosphorene with chemical instability in the atmosphere, the exposure in the atmosphere will further reduce its mechanical properties.

4.2.1 Strain rate. It is believed that the mechanical properties and behaviour of 3D bulk materials deeply depend on strain rates according to the kinetic theory of solid fracture, while 2DLMs evidently amplify their influence due to the ultrathin nanostructure. Generally, fracture strength and strain will be greater at higher strain rate,[146,162,169] which results from that lower strain rate allows more time for the thermal fluctuations of atoms and thus the possibility of bond breaking will increase. Sometimes the effect of chirality should be considered in the sensitivity of mechanical properties to the strain rate.[146,169] But the effect of strain rate to the mechanical properties is weaker than that of temperature. It was found that the strain-rate sensitivity significantly increased with the rise of temperature in silicene, indicating that the fracture stress was less sensitive to the strain rate because of weaker thermal fluctuation of Si atoms at a lower temperature.[162]

4.2.2 Substrate roughness. The substrate roughness used for the growth of 2DLMs is responsible for materials' homogeneity,[191] domain size,[192,193] crystallinity[194] and coverage,[195] which will dramatically impact the mechanical properties. This dependence between roughness of substrates and mechanical properties has been demonstrated to provide another route to tailor the mechanical properties at the growth stage instead of *via* post-process defect engineering methods.[196] The enhanced fracture strength was then confirmed by AFM indentations on graphene sheet grown on electropolished Cu foils. Smoother substrates induced reduction in nucleation density, further allowing for the growth of higher quality graphene.

4.2.3 Chemical instability. Not all 2DLMs can exhibit a strong chemical stability in the atmosphere like graphene. Single- and few-layer phosphorene have been reported to be unstable in the atmosphere because the moisture and oxygen in air can lead to the degradation of phosphorene by oxidation.[197,198] Thus, the Young's modulus and tensile strength of phosphorene were greatly reduced by the passivation layer of phosphorene oxide.[93] But it was worth noting that the significant reduction of Young's modulus upon the exposure time to atmosphere only occurred in the flakes thinner than 6 nm, while the tensile strength for all thickness ranges decreased with the increasing exposure time. This may be attributed to a self-passivation process that saturated with time.

5. Coupling properties

5.1 Electromechanical properties

With the increasing applications of 2DLMs for electronic devices, the influence of electromechanical coupling behaviour on device performance becomes more and more prominent. Not only external electric fields show great influence on mechanical properties of 2DLMs, but also the intrinsic electrical properties of 2DLMs can be tailored by external strain or pressure.

Actually, when a thin nanostructure is exposed to an external electric field, a moment of force arising from the electric polarization effect will be generated and further evoke the nanostructure's deformation as shown in Fig. 19.[199,200] Besides, it has been experimentally observed that the field-induced ripples of graphene can be enhanced by the increase of the transverse electric field.[201] The novel electro-mechanical coupling behaviour stimulates the systematic studies of the effect of electric field on the mechanical properties of 2DLMs. MD calculations revealed that the Young's modulus and fracture stress of graphene under uniaxial tension decreased with the rise of vertical electric potential and net charges.[202] Fracture always originated at the edge of graphene because the increased bond length at the edge of graphene made the edge weaker than the center, which was very different from the case of no fields and charges.[203] Recently, AFM indentation experiments demonstrated that the Young's modulus and fracture strength of suspended graphene with various thicknesses would remain approximately constant until the normalized electric field strength of 0.18 ± 0.03 V nm^{-1} was reached.[204] Fig. 19(e)–(j) show the fracture processes of graphene under different electric field strengths. The excessively regional Joule heating may be the main reason for the fracture of graphene.

Since the electronic properties mainly depend on the band structure, most studies focus on the variation of band structures of 2DLMs during the deformation. Though the carrier mobility of semimetal graphene is ultrahigh,[49] graphene seemed to be less sensitive to applied strains,[56] resulting in that the opened bandgap was too small to significantly promote its applications in semiconductor devices. On the contrary, a wide range of 2DLMs have been reported to possess a tunable electronic and optoelectronic properties with the variation of external strain and show a sizable sensitivity to the applied strain.[54–60,110,111,114,141,161,205–207] DFT calculations revealed that the unstrained TMDs (MX_2; M = Mo, W and X =

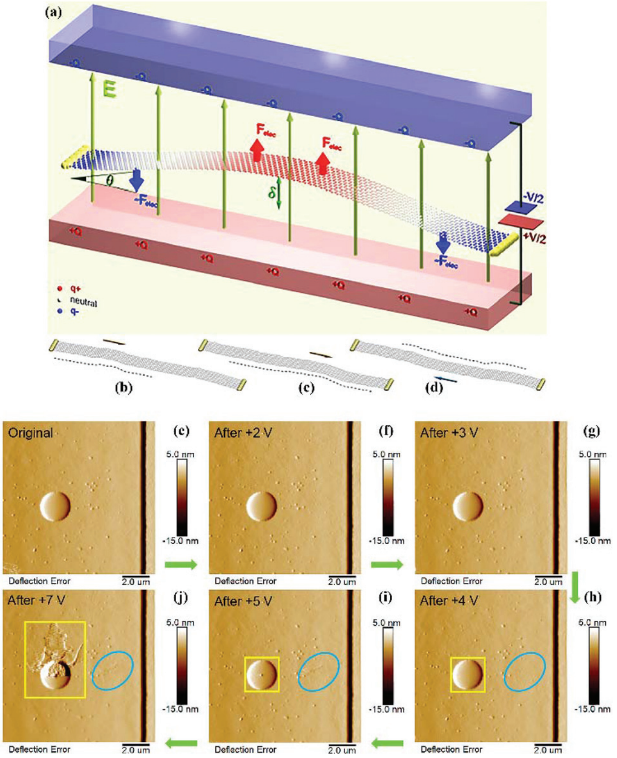

Fig. 19 (a) Topographic diagram of charge distribution on a suspended graphene nanoribbon (GNR) in a transverse electric field *E* from molecular simulations. (b–d) Representative atomic configurations of the graphene at room temperature from MD simulations before the field is applied. (e)–(j) Deflection error maps of graphene nanosheet before and after the conductive AFM nanoindentation process with increasing bias voltages. Reprinted with permission from ref. 199. Copyright 2010 American Physical Society. Reprinted with permission from ref. 204. Copyright 2017 American Chemical Society.

S, Se, Te) possessed semiconducting bandgaps of 1.06–1.81 eV.[56] All these TMDs were very sensitive to the external strains as shown in Fig. 20(a), resulting in the transition of direct-to-indirect band gap and semiconductor-to-metal. The reduction in bandgaps of TMDs was further confirmed by the very recent experiments.[59] Under a three-dimensional pressure, a pressure-induced semiconducting to metallic transition in multilayered MoS_2 was observed at ∼19 GPa owing to the enhanced sulphur–sulphur interactions as the interlayer spacing reduced (shown in Fig. 20(b) and (c)).[208] However, in contrast to the decrease in the bandgaps of TMDs with the increasing strain, the bandgap of γ-graphdiyne kept increasing from 0.28 to 0.71 eV with the character of direct bandgap within the uniform strain ranging from −0.05 to 0.06.[110] Even more complicated variation of bandgaps instead of monotonous changes with external strains have been found in other 2DLMs,[58,111] suggesting that the mechanisms behind vary with the structures of studied materials. While for highly anisotropic materials, the variation of band structures and electronic properties with external strains are also highly anisotropic, such as phosphorene,[57] TiS_3 [60] and T_d-WTe_2.[114]

Except for the band structure, the modulation of the magnetic properties tightly related to lattice structure can also be realized by local strain. By combining experiments with calculations, strain-induced magnetization was confirmed on wrinkle of ReS_2 due to the spin polarization.[102] Besides, the tensile strain can also alter the redistribution of spin-polarized electrons induced by lattice distortion.[209] It was revealed that the local magnetic moments and ferromagnetic stability in graphene with topological line defect were enhanced under tensile strain along the zigzag direction, while diminished under tensile strain along the armchair direction. Moreover,

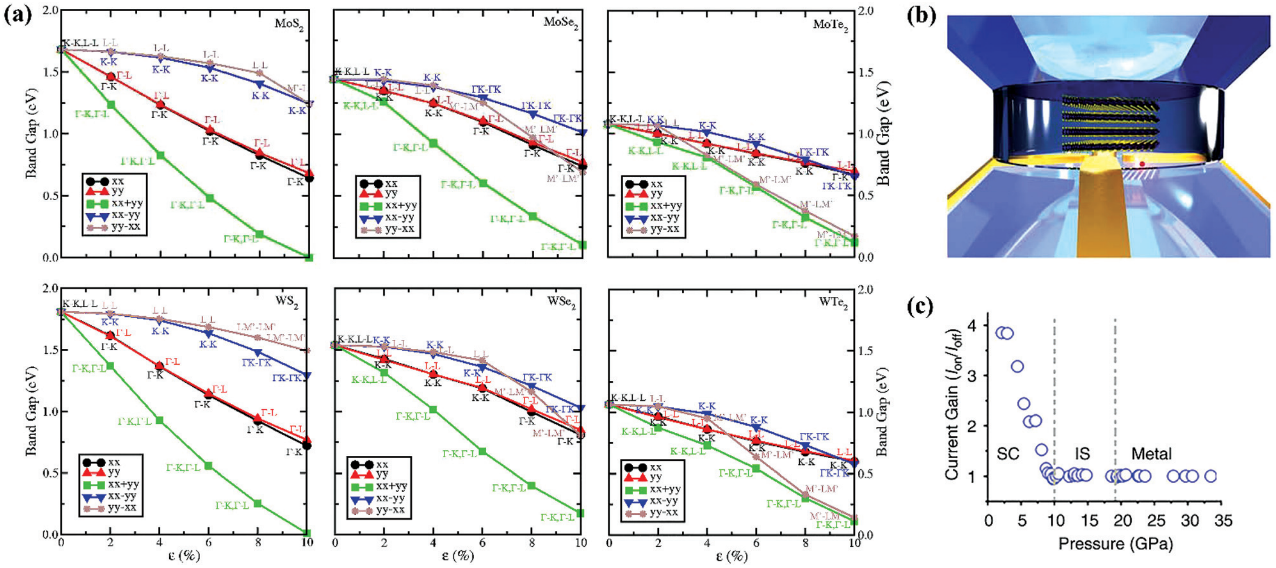

Fig. 20 (a) Band gap of monolayer TMDs with respect to strain, *ε*. (b) A 3D illustration of multilayered MoS_2 in a high-pressure diamond anvil cell (DAC) for compression experiments. (c) Current gain (defined as I_{on}/I_{off} ratio) as a function of pressure when exposed to a 532 nm (2.3 eV) laser light with an intensity of 40 W m^{-2}. Reprinted with permission from ref. 56. Copyright 2012 American Chemical Society. Reprinted with permission from ref. 208. Copyright 2014 Springer Nature.

half-fluorinated BN and GaN exhibited intriguing magnetic transitions between ferromagnetism and antiferromagnetism by strain regulation due to the combined effects of both through-bond and p–p direct interactions.[210] DFT calculations disclosed that pristine VX_2 (X = S, Se) monolayers exhibited a variable exciting ferromagnetic behaviour tuned by isotropic strains, which could be utilized for the design of mechanical switch for spin-polarized transport.[211]

The piezoresistive effect of 2DLMs is an important property that pave the way to nano-scale piezoresistive sensors with high sensitivity. Basically, the piezoresistive behaviour is believed to be a superposition of carrier density and carrier mobility modification.[212] Experiments and simulations on graphene showed that its piezoresistive property depended on whether it was strained uniaxially or biaxially, but was independent of crystallographic orientation and doping concentration.[212,213] Interestingly, the experiments on CVD-grown graphene even reported a strain-dependent resistance where the conductance slightly increased, dramatically decreased and suddenly dropped with the gradual increase of uniaxial strain. This unique behaviour should be attributed to three stages of the relaxation of pre-existing winkles, the elastic deformation and the plastic deformation, respectively.[214] In contrast to graphene, MoS_2 exhibited a negative piezoresistive behaviour, indicating its decreasing resistance with the increasing strain.[215] Furthermore, the piezoresistive property of MoS_2 was suggested to be highly related to the layer number. The studies on black phosphorus indicated the gate doping could also induce huge influence on the piezoresistive response owing to the modulated bandgap.[216] While for highly-anisotropic material like ReS_2, the strain induced broadening and narrowing of the bandgap along two principle directions, resulting in completely opposite piezoresistances (positive and negative).[217]

Piezoelectric effect is of great importance in the applications of sensors[218] and power generation.[219] Specially, when materials with polarization domains or non-centrosymmetric structures are strained along a certain direction, internal polarization will induce heterogeneous charges on opposite surfaces. Due to the absence of an inversion center, single-layer h-BN, group VI TMDs (MX_2, M = Mo, W, Cr and X = S, Se), group IV monochalcogenides (MX, M = Sn, Ge and X = S, Se) are theoretically proposed to exhibit piezoelectricity.[220–224] Though intrinsic graphene was believed to be devoid of piezoelectricity, DFT calculations predicted that doping graphene on one side was a feasible route for gaining piezoelectricity.[225] Experimentally, in-plane piezoelectric effect and out-of-plane piezoelectric effect were obtained in strained/unstrained graphene junction[226] and supported graphene on SiO_2,[227] respectively. It was worth noting that the first experimental observation of piezoelectricity in 2DLMs was in single-layer MoS_2[228] rather than graphene. With the presence of piezoelectric charge, the current–voltage curve of single-layer MoS_2 device shifted leftwards or rightwards under tensile strain or compressive strain, respectively. The detectable piezoelectric effect could only be observed in MoS_2 with an odd number of layers, because flakes with even atomic layers were centrosymmetric owing to the opposite orientation of alternating layers. Further studies[229,230] confirmed this piezoelectric response in monolayer MoS_2, and the piezoelectric polarization was reported to highly depend on its crystal orientation.[230] Similarly, strong piezoresponse was found in WSe_2 odd-layers *via* laterally excited scanning probe microscopy.[231] Though the piezoelectric behaviour in WSe_2 even-layers was negligible,[231] it was interesting that reliable piezoelectric property was obtained from WSe_2 bilayers fabricated by turbostratic stacking.[232]

Since the piezoresistive and piezoelectric effects are critical in tailoring the electromechanical properties of 2DLMs towards applications in electronics, the results of recent simulation and experiments on the piezoresistive and piezoelectric properties are summarized as shown in Table 5.

5.2 Optomechanical properties

Strain-induced modulation of optical properties of 2DLMs provides an effective tool to improve the performance of optoelectronic nanodevices. Herein, the relationship between strain and optical absorption as well as Raman spectroscopy will be discussed.

Experiments on the optical response of graphene showed a constant and universal optical absorption (a transparency of ∼97.7%) over a broad range of frequencies from far-infrared to visible range.[233] When considering the strain-induced anisotropy of the optical conductivity, both experimental and theoretical efforts confirmed the anisotropy of optical absorption in graphene.[234–236] This finding indicated that dichroism and transmittance of graphene were all tunable by external strain, and the applied strain field could be further mapped by two transmittance measurements.[236] By DFT with generalized gradient approximation, anisotropic optical behaviour were observed in monolayer MoS_2, whose reflectivity in the visible region could be modulated from 4% to 10% by compressive and tensile strain.[237] Moreover, external strain could also be employed to tune the optical properties of twisted heterostructures. It was reported that the absorption band of MoS_2/PtS_2 had a red-shift and a broadening effect by ∼350 nm under 5% tensile strain.[238]

The Raman spectroscopy of pristine graphene without defects is mainly characterized by two peaks: G peaks and 2D peaks. The G peak (∼1580 cm^{-1}) originates from the first order signal of in-plane vibrations of carbon atoms, while the 2D peak (∼2700 cm^{-1}) come from the second order double resonance processes.[239] Generally, tensile strain and compressive strain could lead to phonon softening (red shift) and phonon hardening (blue shift), respectively.[240] Besides, both tensile strain and compressive strain were suggested to induce the splitting of G peak into two parts which were typically called G^+ and G^- peak.[32,240–243] Typical strain-induced phonon softening of G peak and 2D peak can be obtained in Fig. 21. Due to the similar hexagonally packed structures of TMDs (MoS_2, $MoSe_2$, WS_2 and WSe_2), theoretical analysis indicated that they have similar optical phonon modes.[244] Here MoS_2 is introduced as an example. There are four first-order Raman-active

Table 5 Piezoresistive and piezoelectric properties of 2DLMs

Material	Fabrication method	Gauge factor	Strain type	Method	Ref.
Piezoresistive properties					
Graphene	—	2.2	Uniaxial	Simulation	212
Graphene	—	1.25	Biaxial	Simulation	212
Graphene	CVD	3.91	Uniaxial	Experiment	212
Graphene	CVD	6.73	Biaxial	Experiment	212
Graphene	CVD	2.92	Pressure	Experiment and simulation	213
MoS_2	—	−43.5 to −224	Uniaxial	Simulation	215
Black phosphorus	—	185	Uniaxial	Experiment	216
ReS_2	Mechanical isolation	50.14	*A*-Axis	Experiment and simulation	217
ReS_2	Mechanical isolation	−60.49	*B*-Axis	Experiment and simulation	217

		Piezoelectric coefficient				
Material	Fabrication method	e_{11} (10^{-10} C m^{-1})	d_{11} (pm V^{-1})	Strain type	Method	Ref.
Piezoelectric properties						
Strained/unstrained graphene junction	Mechanical isolation	—	37 000	Biaxial	Experiment	226
Graphene on SiO_2 calibration grafting substrates	CVD	—	1400	—	Experiment	227
h-BN	—	−1.19	—	—	Simulation	220
h-BN	—	1.38	0.60	Uniaxial	Simulation	221
MoS_2	—	3.64	3.73	Uniaxial	Simulation	221
MoS_2	—	3.62	3.65	Uniaxial	Simulation	224
MoS_2	Mechanical isolation	2.9	—	Uniaxial	Experiment	229
MoS_2	CVD	—	3.78	Armchair	Experiment	230
MoS_2	CVD	—	1.38	Zigzag	Experiment	230
$MoSe_2$	—	3.92	4.72	Uniaxial	Simulation	221
$MoSe_2$	—	3.83	4.55	Uniaxial	Simulation	224
$MoTe_2$	—	5.43	9.13	Uniaxial	Simulation	221
$MoTe_2$		4.67	7.39	Uniaxial	Simulation	224
WS_2	—	2.47	2.19	Uniaxial	Simulation	221
WS_2	—	2.43	2.12	Uniaxial	Simulation	224
WSe_2	—	2.71	2.79	Uniaxial	Simulation	221
WSe_2	—	2.57	2.64	Uniaxial	Simulation	224
WSe_2	Mechanical isolation	—	5.2	—	Experiment	231
WSe_2	CVD	—	3.26	—	Experiment	232
Turbostratic stacking WSe_2	CVD	1.79–1.93	1.08–1.19	—	Experiment and simulation	232
WTe_2	—	3.40	4.60	Uniaxial	Simulation	221
WTe_2	—	3.23	4.39	Uniaxial	Simulation	224
GeS	—	4.6	75.43	Armchair	Simulation	222
GeS	—	−10.1	−50.42	Zigzag	Simulation	222
GeSe	—	12.3	212.13	Armchair	Simulation	222
GeSe	—	−8.2	−97.17	Zigzag	Simulation	222
SnS	—	18.1	144.76	Armchair	Simulation	222
SnS	—	13.8	−22.89	Zigzag	Simulation	222
SnSe	—	34.9	250.58	Armchair	Simulation	222
SnSe	—	10.8	−80.31	Zigzag	Simulation	222
CrS_2	—	4.72	5.36	Uniaxial	Simulation	223
CrS_2	—	5.43	6.15	Uniaxial	Simulation	224
$CrSe_2$	—	5.75	8.25	Uniaxial	Simulation	224
$CrTe_2$	—	6.54	13.45	Uniaxial	Simulation	224
NbS_2	—	2.11	3.12	Uniaxial	Simulation	224
$NbSe_2$	—	2.22	3.87	Uniaxial	Simulation	224
$NbTe_2$	—	1.84	4.45	Uniaxial	Simulation	224
TaS_2	—	2.67	3.44	Uniaxial	Simulation	224
$TaSe_2$	—	2.50	3.94	Uniaxial	Simulation	224
$TaTe_2$	—	2.07	4.72	Uniaxial	Simulation	224

modes in bulk MoS_2 at frequencies of 32 cm^{-1} (E_{2g}^{2}), 286 cm^{-1} (E_{1g}), 383 cm^{-1} (E_{2g}^{1}) and 408 cm^{-1} (A_{1g}),[245,246] while only in-plane E_{2g}^{1} and out-of-plane A_{1g} could be apparently observed because of the Rayleigh scattered laser light and selection rules in backscattering experimental arrangement.[247,248] With the increasing of applied strain, a red-shift was observed in E_{2g}^{1} peak while A_{1g} peak almost stayed unchanged.[247–249] When strain further increased, pristine E_{2g}^{1} would split into two sub-bands as E_{2g}^{1+} and E_{2g}^{1-}.[247,249] The splitting of in-plane mode E′ was also experimentally detected in monolayer CVD WS_2.[250] Black phosphorus with a highly puckered structure possesses six Raman-active modes, but only three of them

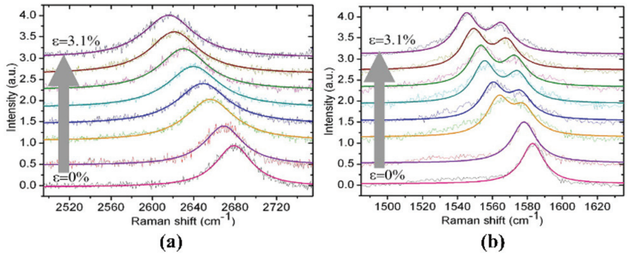

Fig. 21 Strain-induced phonon softening of *G* peak (a) and 2D peak (b) in graphene. Reprinted with permission from ref. 243. Copyright 2009 National Academy of Sciences.

can be observed in the normal backscattering configuration, named $A_g{}^1$ (out-of-plane mode, located at ~361 cm^{-1}), $A_g{}^2$ (in-plane mode, located at 467 cm^{-1}) and B_{2g} (in-plane mode, located at 438 cm^{-1}), respectively.[251–254] Previous theoretical and experimental studies have measured the angle-dependent Raman shifts induced by uniaxial strain, where $A_g{}^1$ mode was more sensitive to strain along the near-armchair direction whereas $A_g{}^2$ and B_{2g} were more sensitive to strain along the near-zigzag direction.[255,256]

5.3 Thermomechanical properties

Due to the atomically-thin structure of 2DLMs, their mechanical properties are more sensitive to temperature than 3D bulk materials. Theoretically, thermomechanical properties should be investigated under the analysis of the evolution of atomic structures during the change of thermal environments. In general, their in-plane mechanical properties are believed to be softened with the increasing of temperature. This temperature-induced softening can be understood from the following three aspects.[132,135,162,173] Firstly, the equilibrium distance between atoms will increase with the increasing temperature, which indicates that the initial bond length is larger at higher temperatures. As a result, it is easier to reach the critical bond length for fracture during tensile deformation. Secondly, the enhanced thermal vibrations of atoms at a higher temperature will induce a larger fluctuation of bond length, thus increasing the possibility of some bonds to reach the critical bond length for breaking. Thirdly, higher temperatures will strengthen the fluctuations of out-of-plane ripples, further weakening the Young's modulus of materials. So far, this temperature-induced softening effect has been reported in graphene,[257–259] graphane,[111] phosphorene,[132] h-BN,[135,139] silicene,[162] Bi_2Te_3 [173] and graphene/silicene/graphene heterostructures.[146]

5.4 Strain-induced phase transitions

Strain-induced phase transitions of 2DLMs are of great importance in their applications towards phase-change electronics. In contrast to graphene, group VI TMDs usually have more than one possible crystal structure (shown in Fig. 22) consisting of semiconducting phase (2H phase) and metal phase (1T phase and 1T′ phase), but only 2H phase and 1T′ phase are stable without external stabilizing influences.[260] Interestingly, group VI TMDs all exhibit 2H phase under ambient conditions except WTe_2 which is 1T′ phase.[260,261] Theoretical calculations have demonstrated that though the phase transition from 2H phase to 1T′ phase could occur in MoS_2, $MoSe_2$, $MoTe_2$, WS_2 and WSe_2 by biaxial strain, the transition strain may be below but near their breaking thresholds.[260,262] While for WTe_2, compressive strain could be employed to arouse the phase transition from 1T′ phase to 2H phase.[260,262] Due to the lower threshold strain for phase transition, experimental observation of this transition has been reported to be accessible in $MoTe_2$.[263] The property that coherent spin transport can occur without heat dissipation in 2D topological insulators makes them ideal materials for dissipationless devices. Previous study has indicated that the monolayer TMDs in 1T′ phase, H′ phase, and T″ phase were all topological states.[264–266] Furthermore, by the introducing of defects and equi-biaxial tensile strain, these 2H-phase TMDs could all be changed into topological insulating states.[267] Similarly, the phase transition from ground state to topological phase was theoretically reported to be occurred in few-layers phosphorene under uniaxial compressive strain or vertical tensile strain[268] and experimentally observed in bilayer stacked phosphorene under in-plane compressive strain along either zigzag or armchair direction.[269] It was interesting to note that this phase transition in bilayer phosphorene also depended on the interlayer stacking order. Besides the transition to topological states, first-principles calculations further revealed that the normal compressive strain or anisotropic biaxial in-plane strain could induce structural transition from pristine Z-phosphorene to A-phosphorene.[270]

6. Applications

Mechanical and coupling properties of 2DLMs are the cornerstones towards their applications in flexible and novel electronics, which opens the door to achieve reliable and controllable performances in nano-scale devices. Herein, recent achievements in flexible devices based on unique mechanical properties and novel devices based on coupling properties are briefly introduced and summarized.

6.1 Electronics based on mechanical properties

Theoretically, the properties of high strain limit (generally larger than 10%, see Fig. 14), high mobility (comparable to Si and even larger[271]), widely varing electronic properties (from metal to insulator[272]) and excellent combinability (heterostructural electronics by relatively strong van der Waals interaction[137,273,274]) generate great interest for the fabrication and application of flexible electronics including transistors, electrodes and photodetectors.

Earlier reports on flexible transistors are mainly related to graphene with an ultrahigh mobility of up to 10 000 cm^2 V^{-1} s^{-1}.[271] Lee and coworkers[275] fabricated rugged multi-finger embedded-gate graphene field-effect transistors (EGFET) on flexible polyimide (PI) sheets (shown in Fig. 23(a)) whose

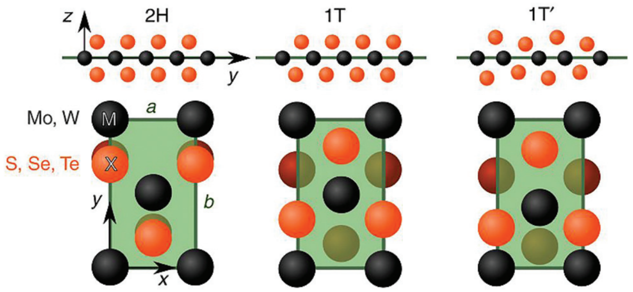

Fig. 22 Possible crystal structures of 2D group VI TMDs. Reprinted with permission from ref. 260. Copyright 2014 Springer Nature.

robust electrical performance maintained down to a bending radius of ~1.3 mm corresponding to a bending strain of ~4.6%. Later report indicated the mechanical robustness of graphene field-effect transistors (GFETs) on flexible PI substrates could be even improved to 0.7 mm bending radius.[276] Repeated measurements under the minimum bending radius of 0.7 mm further confirmed its mechanical and electrical reliability. However, the lack of natural bandgap in graphene stimulates the exploration of other 2D layered semiconducting materials, including TMDs (bandgap: 1.06–1.81 eV (ref. 56)) and phosphorene (bandgap: 1.51 eV (ref. 277)). By using mechanically exfoliated MoS_2 as channel material, flexible MoS_2 transistors on industrial plastic sheets (shown in Fig. 23(b)) were fabricated and exhibited an on/off ratio of larger than 10^7, a mobility of ~30 $cm^2\ V^{-1}\ s^{-1}$ and a subthreshold slope of ~82 mV per decade in the atmosphere.[278] Bending measurements indicated that the deteriorated properties caused by the fracture of dielectrics (Al_2O_3 and HfO_2) only occurred in bending radius smaller than 1 mm. Intriguingly, the interlayer van der Waals interaction of 2D heterostructure is sufficient to maintain their structural stability,[38] thus allowing for the fabrication of mechanically reliable heterostructural transistors. Combining the high mobility of graphene and the semiconducting property of MoS_2, Yoon *et al.*[273] developed a highly flexible and transparent transistor (shown in Fig. 23(c)) with a high on/off ratio (>10^4) and an average mobility of ~4.7 $cm^2\ V^{-1}\ s^{-1}$ by using CVD grown graphene as source/drain electrodes and exfoliated MoS_2 as channels. The electronic properties were stable up to bending radius of ±2.2 mm in compressive and tensile modes, even though a small deterioration was observed after bending cycles of up to 10 000 between bending radii of ∞ to 2.7 mm in tensile mode. Furthermore, an ultrathin transistor was developed only by mechanical stacking of conducting graphene (gate electrode), insulating h-BN (dielectric) and semiconducting MoS_2 (channel) as shown in Fig. 23(d).[137] The resulted mobilities of up to 45 $cm^2\ V^{-1}\ s^{-1}$ and operating gate voltage below 10 V combined with the excellent electrical robustness upon external strain (up to 1.5%) made it possible for the realization of high-performance flexible and transparent transistors with ultra-small size. Except graphene and TMDs, recent work[279] has reported the first flexible field-effect transistor based on few-layer phosphorene, a new semiconducting 2D material, with a maximum carrier mobility of ~310 $cm^2\ V^{-1}\ s^{-1}$, which was much larger than ever reported transistors based on MoS_2[278] and WSe_2.[274] More importantly, such high mobility was stable up to 2% uniaxial tensile strain and up to 5000 bending cycles.

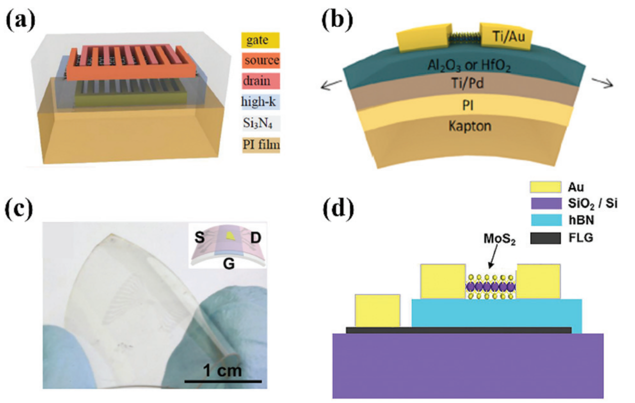

Fig. 23 (a) 3D image of multi-finger EGFET of a 10-finger unit cell. (b) Schematic depiction of flexible bottom gate transistor based on MoS_2. (c) Photograph image of the highly flexible and transparent MoS_2 transistors on a PET substrate. (d) Schematic device structure of transistor by mechanical stacking of graphene, h-BN and MoS_2. Reprinted with permission from ref. 275. Copyright 2012 AIP Publishing. Reprinted with permission from ref. 278. Copyright 2013 American Chemical Society. Reprinted with permission from ref. 273. Copyright 2013 John Wiley and Sons. Reprinted with permission from ref. 137. Copyright 2013 American Chemical Society.

For non-transistor applications, graphene has been proved to be ideal candidate for stretchable transparent electrodes with high conductance and high flexibility.[49] The resistance of graphene electrode exhibited no evident variation up to bending radius of 2.3 mm corresponding to uniaxial tensile strain of 6.5%, whereas the pre-strained substrates could improve the bending limit up to ~11%. On the other hand, novel photodetectors with high performance and high flexibility also benefit from the development of 2D layered semiconducting materials. For example, photodetector based on large-area and highly-crystalline WSe_2 prepared by pulsed-laser deposition possessed an ultra-broadband detection spectral range from 370 to 1064 nm, reversible photoresponsivity of ~0.92 $A\ W^{-1}$ and external quantum efficiency of up to 180%.[138] The corresponding optoelectronic property of the device under constant incident light intensity and various bending radii showed almost no change even at a radius of 5 mm.

6.2 Electronics based on coupling properties

The piezoresistive property of 2DLMs gives rise to ultrathin strain sensor with high flexibility and sensitivity, which can be directly used to detect external strain or pressure. More complicated strain can be detected when strain sensors are fabricated into an array, further demonstrating their applicability in electrical skins for robotics and human body motion monitoring.[280–283] Due to the large strain limit, high electrical conductance and excellent transparency of graphene, a great deal of studies on graphene based strain sensors have been carried out. Among these results, their gauge factor differed from −2 to 10^6 due to the different synthetic methods, substrates, structural forms and so on.[284,285] Ahn *et al.*[286] fabricated wafer-scale graphene *via* CVD method, and the transferred graphene showed a gauge factor (GF) of 6.1. In order to detect the bending motion of a finger, three identical strain sensors in a rosette manner (shown in Fig. 24(a)) were further fabricated on a wearable and stretchable glove, which could simultaneously detect both force and strain direction.[287] Zhang *et al.*[288] firstly proposed a charge tunneling model for the piezoresistive effect of a high GF more than 300 in nanographene (NG) films grown in a remote plasma enhanced chemical vapor deposition (RPECVD) system. Intriguingly, different nucleation of NG providing various initial tunneling distances between NG sheets could be tuned by temperature, leading to the GF of NG devices varying from 10 to 10^3 with the same resistance.[289] Besides, they designed periodical ripples of NG to further improve the strain limit (>30%) for flexible electronic applications (shown in Fig. 24(b)).[284] On the other hand, Zhu *et al.* obtained an ultrahigh GF of ∼10^6 by employing graphene woven fabrics as strain sensors, which could detect weak body motions as electronic skins, including hand clenching, phonation, expression change, blink, breath, and pulse.[281,285] For fabricating large-area ultrathin graphene *via* an environment-friendly and cost-effective method, Zhu *et al.* proposed a self-assembly process which was rapid and applicable.[290] Besides, other efforts have also been proved effect routes to improve the sensitivity and stretchiness of graphene based strain sensors. It was reported that new types of graphene strain sensors based on stretchable yarns could detect both large- and small-scale human motions.[291] By using a serpentine-shaped pattern (shown in Fig. 24(c)), the strain sensor was capable of stretching up to 20% with a high GF (42.2) for detecting strain induced by stretching, bending, and torsion.[292] Except graphene, strain sensors based on other 2DLMs have been investigated recently, such as MoS_2,[282,293] α-In_2Se_3 [283] and $PtSe_2$.[294] Unlike traditional two terminal strain sensor, flexible MoS_2 FET strain sensor made the piezoresistivity gate-tunable by more than 1 order of magnitude.[293] Furthermore, the electronic-skin based on strain sensor array of MoS_2 [282] (shown in Fig. 24(d)) and α-In_2Se_3 [283] both exhibited comparable performances to graphene based electronic-skin. Detail information of these strain sensors discussed above is summarized for comparative analysis in Table 6.

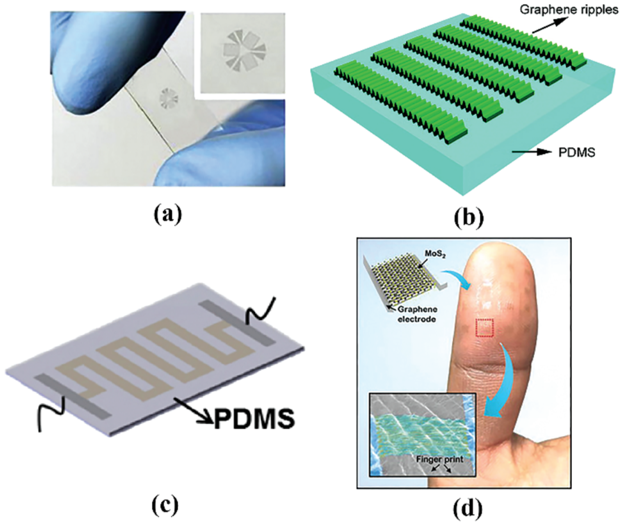

Fig. 24 Graphene strain sensor in a rosette manner. (b) Strain sensor based on graphene ripples. (c) Serpentine-shaped graphene strain sensor. (d) Illustration of MoS_2-based tactile sensor. Reprinted with permission from ref. 287. Copyright 2013 Elsevier. Reprinted with permission from ref. 284. Copyright 2011 American Chemical Society. Reprinted with permission from ref. 292. Copyright 2017 Elsevier. Reprinted with permission from ref. 282. Copyright 2016 John Wiley and Sons.

Table 6 Comparative parameters of strain sensor based on 2DLMs

Material	Fabrication method	Dimension (μm × μm)	Layer	Substrate	Strain (%)	GF	Sensitivity ($mbar^{-1}$)	Ref
Graphene	CVD	300 × 140000	1	PDMS	1	6.1	—	286
Graphene	Mechanical exfoliation	1.5 × 22.8	—	PDMS	20	−2	—	284
NG	Mechanical exfoliation	—	—	PDMS	30	0.55	—	284
Graphene	CVD	750 × 750	1	Si_xN_y	2.5×10^{-4}	1.8×10^4	—	302
NG	RPECVD	2 × 1400	—	Mica	0.3	300	—	288
Graphene	CVD	—	—	PDMS	7	10^6	—	285
Graphene	CVD	6 × 64	1	Suspended	0.29	2.92	2.96×10^{-6}	237
Graphene	CVD	280 × 280	Multilayer	SiN_x	0.25	1.6	6.67×10^{-6}	303
Graphene	CVD	—	10	PDMS	2	2.4	—	287
Graphene	Direct reduction of GO	20 × 600	—	PET	—	9.49	—	304
NG	RPECVD	500 × 500	—	PDMS	1	500	—	289
Graphene	CVD	490 × 490	6	SiN_x	0.22	4.4	2.8×10^{-5}	305
Graphene	Self-assembly	—	4.4 nm	PDMS	2	1037	—	290
Graphene	CVD	—	1	PDMS	20	42.2	—	292
MoS_2	Direct sulfurization	—	3	Al_2O_3/ITO/PET	0.1	−40	—	293
MoS_2	CVD	1850 × 2100	2	SU-8	−1.98;1.98	−72.5; −56.5	—	282
α-In_2Se_3	CVD	500 × 1900	9.1 nm	PET	0.39	237	—	283
$PtSe_2$	TAC	—	7–8	Suspended	—	−84.8	5.51×10^{-4}	294

The piezoelectric properties of 2DLMs have been utilized for the applications of nanogenerator,[226,228,230,232,295] phototransistor,[296] strain/pressure sensor[297] and actuator.[298] Previous experiment has demonstrated monolayer MoS_2 strained by 0.53% could generate a peak output of 15 mV and 20 pA with a power density of 2 mWm^{-2} and an energy conversion efficiency of 5.08%.[228] When these CVD grown MoS_2 flakes were fabricated into array integrations (shown in Fig. 25(a)), great enhancements were acquired in output voltages or currents for four MoS_2 nanosheets connected in series or parallel, respectively.[228] Besides, the piezoelectric effects in CVD grown MoS_2 were reported to be directional dependent, resulting in the two times higher output power of nanogenerator with the armchair direction than with the zigzag direction.[230] Though CVD is an ideal method for controllable large-area growth of ultrathin MoS_2, sulfur vacancies are inevitable formed to screen piezoelectric polarization charges.[295] For improving the performances of CVD grown MoS_2 nanogenerator (shown in Fig. 25(b)), sulfur S passivation was proposed and proven to increase the output peak current and voltage by more than 3 times (100 pA) and 2 times (22 mV), respectively.[295] Recent observation of the band-piezoelectric effect of biaxial-strained graphene, which arises from the charge transfer along a work function gradient, provides a versatile platform for graphene based nanogenerator.[226] The obtained energy conversion efficiency was estimated to be 2.2%. Due to the absent piezoelectric effect in pristine bilayer TMDs, turbostratic stacking was proposed to achieve reliable energy harvesting performance in WSe_2 by inducing noncentrosymmetry and increasing mechanical durability.[232] The harvesting energy of integrated WSe_2 nanogenerators were even able to operate a small liquid crystal display (LCD) without external bias. Further study demonstrated that the piezoelectric effect could be utilized to modulate the carrier dynamics, resulting in strain-gated MoS_2 phototransisitor with smallest photocurrent for uniaxial strain of 0.62% and largest photocurrent for uniaxial strain of −0.38%.[296] Additionally, the polarization charges could alter the Schottky barrier height on the contacts of MoS_2 devices, which was used to realize controllable modulation of the conductivity under strain variation.[297] The reliable strain-gating electrical transport gave rise to a new type of MoS_2 strain sensor with a high GF of ∼1160. Apart from the in-plane piezoelectricity discussed above, the vertical piezoelectricity in 2DLMs is a key property of their application as actuators with high accuracy of nanometer scale, which is an important part in equipment like force atomic microscopy and scanning tunneling microscopy. Very recent study has measured the vertical piezoelectric coefficient of ultrathin CdS films to be 33 pm V^{-1}.[298] The FEM simulation of this novel actuator revealed that the deformation of CdS film was linearly increase from ∼30 to ∼150 pm when the driven voltage varied from −1 to −5 V.

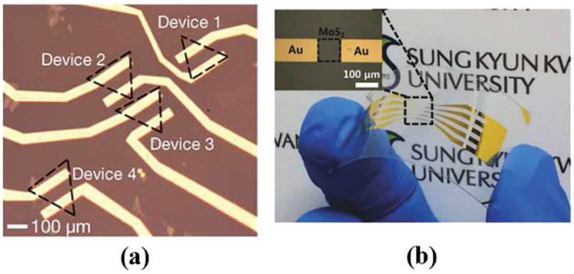

Fig. 25 (a) Array integration of CVD single-layer MoS_2 flakes as nanogenerators. (b) MoS_2 based flexible nanogenerator on a PET substrate. Reprinted with permission from ref. 228. Copyright 2014 Springer Nature. Reprinted with permission from ref. 295. Copyright 2018 John Wiley and Sons.

It was reported that the strain-induced wrinkles of 2DLMs could enhance their photoabsorption because of areal densification, and consequently flexible strain-tunable photoresponsivity could be realized in their photodetectors.[299,300] Specially, the enhanced optical extinction by more than 12.5 times accounted for the enhancement of ∼370% in photoresponsivity of crumpled graphene photodetector compared with a flat graphene photodetector.[299] Besides, the strain-induced enhanced photoabsorption in MoS_2 was also confirmed by ultraviolet–visible spectroscopy.[299] Furthermore, the plasmonic enhancement by gold nanoparticle in crumpled graphene could increase the photoresponsivity even by ∼1200%, suggesting the potential applications of this stretchable photodetector as flexible optical sensor and strain sensor.[300]

7. Conclusions and outlooks

In this review, we have summarized the basic mechanical and coupling properties of novel 2DLMs from comprehensive aspects including characterization methods, intrinsic mechanical properties and behaviour, influence factors, coupling properties and related electronic applications. During the exploration to these atomic thin materials, a great deal of intriguing discoveries have been reached and further stimulated more focus on the fundamental physics and engineering applications. For example, the combined properties of high strength and high flexibility of 2DLMs make them possible not only for the development of flexible and transparent nanodevices based on inorganic low-dimensional materials but also for the regulation of their electronic properties in a relative wide range. Besides, coupling properties between mechanical properties and other physical properties further pave the way to novel nanodevices with unique properties. On the other hand, the close relationship between mechanical properties and internal defects or external environments provides an effective route to tailor 2DLMs with ideal mechanical properties by local regulation or overall regulation.

However, the progress made today is far away from the way to final goal. As most studies have demonstrated, perfect 2DLMs always exhibit a brittle behaviour which induces difficulties in their fabrication and usage, because any small defects introduced may cause a great deterioration of strength and failure strain. Even though some efforts have been paid to improve their fracture toughness by defects engineering or chemical functionalization, this problem has not been well solved. Besides, note that some studies have proven that continuum mechanics and related theories are applicable to 2DLMs, but there is still a doubt whether the results from continuum mechanics are reliable for all 2DLMs. And how to bridge the gap between continuum mechanics and atomic level analysis will be the next challenge. In addition, the mechanical properties and mechanical behaviour of graphene, MoS_2, h-BN and phosphorene have been investigated systematically, but a great deal of other 2DLMs (more than 30 kinds of 2D materials have been synthesized just for TMDs[301]) are yet to be studied. Furthermore, some achievements of the coupling properties in this field are proposed only by theoretical analysis without experimental observations, which may be due to the difficulty in experimental operations. So more efforts need to make it clear the real states of coupling properties and make these coupling properties more accessible and controllable in their applications.

Overall, understanding and mastering the mechanical and coupling properties of 2DLMs are of great importance for better design, fabrication and usage of their nanodevices. We hope this review will provide the basic points of progress in this field over the past few years. But it should be noted that more efforts still need to be applied to set up the blocks for this field from fundamental theories and engineering applications.

Conflicts of interest

There are no conflicts to declare.

Acknowledgements

This research is financially supported by the National Natural Science Foundation of China (Grant No. 51527901 and 51475256), the National Key Research and Development Program of China (2018YFB2000202), and Beijing National Science Foundation of China (grant no. 3182010).

Notes and references

1 A. K. Geim and K. S. Novoselov, *Nat. Mater.*, 2007, **6**, 183–191.
2 Y. Zhang, Y. W. Tan, H. L. Stormer and P. Kim, *Nature*, 2005, **438**, 201–204.
3 C. Berger, Z. M. Song, X. B. Li, X. S. Wu, N. Brown, C. Naud, D. Mayou, T. B. Li, J. Hass, A. N. Marchenkov, E. H. Conrad, P. First and W. A. D. Heer, *Science*, 2006, **312**, 1191–1196.
4 C. Lee, X. Wei, J. W. Kysar and J. Hone, *Science*, 2008, **321**, 385–388.
5 K. Bolotin, K. J. Sikes, Z. F. Jiang, M. Klima, G. Fudenberg, J. Hone, P. Kim and H. L. Stormer, *Solid State Commun.*, 2008, **146**, 351–355.
6 G. Q. Ning, Z. J. Fan, G. Wang, J. S. Gao, W. Z. Qian and F. Wei, *Chem. Commun.*, 2011, **47**, 5976–5978.
7 C. R. Dean, A. F. Young, I. Meric, C. Lee, L. Wang, S. Sorgenfrei, K. Watanabe, T. Taniguchi, P. Kim, K. L. Shepard and J. Hone, *Nat. Nanotechnol.*, 2010, **5**, 722–726.
8 T. Palacios, *Nat. Nanotechnol.*, 2011, **6**, 464–465.
9 F. N. Xia, T. Mueller, Y. M. Lin, A. V. Garcia and P. Avouris, *Nat. Nanotechnol.*, 2009, **4**, 839–843.
10 T. Mueller, F. N. Xia and P. Avouris, *Nat. Photonics*, 2010, **4**, 297–301.
11 C. H. Liu, Y. C. Chang, T. B. Norris and Z. H. Zhong, *Nat. Nanotechnol.*, 2014, **9**, 273–278.
12 J. S. Bunch, A. M. van der Zande, S. S. Verbridge, I. W. Frank, D. M. Tanenbaum, J. K. Parpia, H. G. Craighead and P. L. McEuen, *Science*, 2007, **315**, 490–493.
13 J. T. Robinson, M. Zalalutdinov, J. W. Baldwin, E. S. Snow, Z. Q. Wei, P. Sheehan and B. H. Houston, *Nano Lett.*, 2008, **8**, 3441–3445.
14 C. Y. Chen, S. Rosenblatt, K. I. Bolotin, W. Kalb, P. Kim, I. Kymissis, H. L. Stormer, T. F. Heinz and J. Hone, *Nat. Nanotechnol.*, 2009, **4**, 861–867.
15 V. Singh, S. J. Bosman, B. H. Schneider, Y. M. Blanter, A. C. Gomez and G. A. Steele, *Nat. Nanotechnol.*, 2014, **9**, 820–824.
16 M. S. Stoller, S. J. Park, Y. W. Zhu, J. H. An and R. S. Ruoff, *Nano Lett.*, 2008, **8**, 3498–3502.
17 E. J. Yoo, J. Kim, E. Hosono, H. S. Zhou, T. Kudo and I. Honma, *Nano Lett.*, 2008, **8**, 2277–2282.
18 G. X. Wang, X. P. Shen, J. Yao and J. Park, *Carbon*, 2009, **47**, 2049–2053.
19 M. A. Rafiee, J. Rafiee, Z. Wang, H. H. Song, Z. Z. Yu and N. Koratkar, *ACS Nano*, 2009, **3**(12), 3884–3890.
20 Z. Xu and C. Gao, *Macromolecules*, 2010, **43**(16), 6716–6723.
21 X. Zhao, Q. H. Zhang and D. J. Chen, *Macromolecules*, 2010, **43**, 2357–2363.
22 B. Das, K. E. Prasad, U. Ramamurty and C. N. R. Rao, *Nanotechnology*, 2009, **20**, 125705.
23 X. Wang, W. Y. Xing, P. Zhang, L. Song, H. Y. Yang and Y. Hu, *Compos. Sci. Technol.*, 2012, **72**, 737–743.
24 L. S. Walker, V. R. Marotto, M. A. Rafiee, N. Koratkar and E. L. Corral, *ACS Nano*, 2011, **5**, 3182–3190.
25 L. Kvetková, A. Duszová, P. Hvizdoš, J. Dusza, P. Kun and C. Balázsi, *Scr. Mater.*, 2012, **66**, 793–796.
26 J. Y. Wang, Z. Q. Li, G. L. Fan, H. H. Pan, Z. X. Chen and D. Zhang, *Scr. Mater.*, 2012, **66**, 594–597.
27 X. Gao, H. Y. Yue, E. Guo, H. Zhang, X. Y. Lin, L. H. Yao and B. Wang, *Mater. Des.*, 2016, **94**, 54–60.
28 Y. Han, Z. Xu and C. Gao, *Adv. Funct. Mater.*, 2013, **23**, 3693–3700.
29 E. J. Duplock, M. Scheffler and P. J. D. Lindan, *Phys. Rev. Lett.*, 2004, **92**, 225502.

30 R. Balog, B. Jørgensen, L. Nilsson, M. Andersen, E. Rienks, M. Bianchi, M. Fanetti, E. Lægsgaard, A. Baraldi, S. Lizzit, Z. Sljivancanin, F. Besenbacher, B. Hammer, T. G. Pedersen, P. Hofmann and L. Hornekær, *Nat. Mater.*, 2010, **9**, 315–319.

31 Y. B. Zhang, T. T. Tang, C. Girit, Z. Hao, M. C. Martin, A. Zettl, M. F. Crommie, Y. R. Shen and F. Wang, *Nature*, 2009, **459**, 820–823.

32 Z. H. Ni, T. Yu, Y. H. Lu, Y. Y. Wang, Y. P. Feng and Z. X. Shen, *ACS Nano*, 2008, **2**, 2301–2305.

33 G. Cocco, E. Cadelano and L. Colombo, *Phys. Rev. B: Condens. Matter Mater. Phys.*, 2010, **81**, 241412.

34 S. Park, K. Lee, G. Bozoklu, W. Cai, S. T. Nguyen and R. S. Ruoff, *ACS Nano*, 2008, **2**, 572–578.

35 D. C. Elias, R. R. Nair, T. M. G. Mohiuddin, S. V. Morozov, P. Blake, M. P. Halsall, A. C. Ferrari, D. W. Boukhvalov, M. I. Katsnelson, A. K. Geim and K. S. Novoselov, *Science*, 2009, **323**, 610–613.

36 G. X. Li, Y. L. Li, H. B. Liu, Y. B. Guo, Y. J. Li and D. B. Zhu, *Chem. Commun.*, 2010, **46**, 3256–3258.

37 B. G. Kim and H. J. Choi, *Phys. Rev. B: Condens. Matter Mater. Phys.*, 2012, **86**, 115435.

38 A. K. Geim and I. V. Grigorieva, *Nature*, 2013, **499**, 419–425.

39 Y. W. Zhu, S. Murali, W. W. Cai, X. S. Li, J. W. Suk, J. R. Potts and R. S. Ruoff, *Adv. Mater.*, 2010, **22**, 3906–3924.

40 P. Cudazzo, C. Attaccalite, I. V. Tokatly and A. Rubio, *Phys. Rev. Lett.*, 2010, **104**, 226804.

41 K. Srinivasu and S. K. Ghosh, *J. Phys. Chem. C*, 2012, **116**, 5951–5956.

42 Q. H. Wang, K. K. Zadeh, A. Kis, J. N. Coleman and M. S. Strano, *Nat. Nanotechnol.*, 2012, **7**, 699–712.

43 F. N. Xia, H. Wang and Y. C. Jia, *Nat. Commun.*, 2014, **5**, 4458.

44 G. H. Lee, Y. J. Yu, C. G. Lee, C. Dean, K. L. Shepard, P. Kim and J. Hone, *Appl. Phys. Lett.*, 2011, **99**, 243114.

45 H. Wang, F. Liu, W. Fu, Z. Y. Fang, W. Zhou and Z. Liu, *Nanoscale*, 2014, **6**, 12250–12272.

46 C. Zhi, Y. Bando, C. C. Tang, H. Kuwahara and D. Golberg, *Adv. Mater.*, 2009, **21**, 2889–2893.

47 Y. Wang, Z. X. Shi and J. Yin, *J. Mater. Chem.*, 2011, **21**, 11371–11377.

48 A. N. Obraztsov, E. A. Obraztsova, A. V. Tyurnina and A. A. Zolotukhin, *Carbon*, 2007, **45**, 2017–2021.

49 K. S. Kim, Y. Zhao, H. Jang, S. Y. Lee, J. M. Kim, K. S. Kim, J. H. Ahn, P. Kim, J. Y. Choi and B. H. Hong, *Nature*, 2009, **457**, 706–710.

50 C. S. Ruiz-Vargas, H. L. Zhuang, P. Y. Huang, A. M. van der Zande, S. Garg, P. L. McEuen, D. A. Muller, R. G. Hennig and J. Park, *Nano Lett.*, 2011, **11**, 2259–2263.

51 Z. D. Sha, Q. X. Pei, Y. Y. Zhang and Y. W. Zhang, *Nanotechnology*, 2016, **27**, 315704.

52 F. Banhart, J. Kotakoski and A. V. Krasheninnikov, *ACS Nano*, 2011, **5**, 26–41.

53 Q. B. Zheng, Y. Geng, S. J. Wang, Z. G. Li and J. K. Kim, *Carbon*, 2010, **48**, 4315–4322.

54 R. Qin, C. H. Wang, W. J. Zhu and Y. L. Zhang, *AIP Adv.*, 2012, **2**, 022159.

55 M. Ghorbani-Asl, S. Borini, A. Kuc and T. Heine, *Phys. Rev. B: Condens. Matter Mater. Phys.*, 2013, **87**, 235434.

56 P. Johari and V. B. Shenoy, *ACS Nano*, 2012, **6**, 5449–5456.

57 R. X. Fei and L. Yang, *Nano Lett.*, 2014, **14**, 2884–2889.

58 M. Elahi, K. Khaliji, S. M. Tabatabaei, M. Pourfath and R. Asgari, *Phys. Rev. B: Condens. Matter Mater. Phys.*, 2015, **91**, 115412.

59 R. Frisenda, M. Drüppel, R. Schmidt, S. M. D. Vasconcellos, D. P. D. Lara, R. Bratschitsch, M. Rohlfing and A. C. Gomez, *npj 2D Mater. Appl.*, 2017, **1**, 10.

60 R. Biele, E. Flores, J. R. Ares, C. Sanchez, I. J. Ferrer, G. R. Bollinger, A. C. Gomez and R. D'Agosta, *Nano Res.*, 2018, **11**, 225–232.

61 X. D. Wei, B. Fragneaud, C. A. Marianetti and J. W. Kysar, *Phys. Rev. B: Condens. Matter Mater. Phys.*, 2009, **80**, 205407.

62 R. C. Cooper, C. Lee, C. A. Marianetti, X. D. Wei, J. Hone and J. W. Kysar, *Phys. Rev. B: Condens. Matter Mater. Phys.*, 2013, **87**, 035423.

63 A. Castellanos-Gomez, V. Singh, H. S. J. van der Zant and G. A. Steele, *Ann. Phys.*, 2015, **527**, 27–44.

64 K. Liu and J. Q. Wu, *J. Mater. Res.*, 2016, **31**, 832–844.

65 D. Akinwande, C. J. Brennan, J. S. Bunch, P. Egberts, J. R. Felts, H. J. Gao, R. Huang, J. S. Kim, T. Li, Y. Li, K. M. Liechti, N. S. Lu, H. S. Park, E. J. Reed, P. Wang, B. I. Yakobson, T. Zhang, Y. W. Zhang, Y. Zhou and Y. Zhu, *Extreme Mech. Lett.*, 2017, **13**, 42–77.

66 J. H. Kim, J. H. Jeong, N. Kim, R. Joshi and G. H. Lee, *J. Phys. D: Appl. Phys.*, 2018, **52**, 083001.

67 D. G. Papageorgiou, I. A. Kinloch and R. J. Young, *Prog. Mater. Sci.*, 2017, **90**, 75–127.

68 C. Androulidakis, K. Zhang, M. Robertson and S. Tawfick, *2D Mater.*, 2018, **5**, 032005.

69 J. S. Bunch, S. S. Verbridge, J. S. Alden, A. M. van der Zande, J. M. Parpia, H. G. Craighead and P. L. McEuen, *Nano Lett.*, 2008, **8**, 2458–2462.

70 P. Zhang, L. L. Ma, F. F. Fan, Z. Zeng, C. Peng, P. E. Loya, Z. Liu, Y. J. Gong, J. N. Zhang, X. X. Zhang, P. M. Ajayan, T. Zhu and J. Lou, *Nat. Commun.*, 2014, **5**, 3782.

71 X. L. Wei, S. Xiao, F. X. Li, D. M. Tang, Q. Chen, Y. Bando and D. Golberg, *Nano Lett.*, 2015, **15**, 689–694.

72 C. H. Cao, M. Daly, B. Chen, J. Y. Howe, C. V. Singh, T. Filleter and Y. Sun, *Nano Lett.*, 2015, **15**, 6528–6534.

73 S. S. Wang, Z. Qin, G. S. Jung, F. J. M. Martinez, K. Zhang, M. J. Buehler and J. H. Warner, *ACS Nano*, 2016, **10**, 9831–9839.

74 Y. C. Yang, X. Li, M. R. Wen, E. Hacopian, W. B. Chen, Y. J. Gong, J. Zhang, B. Li, W. Zhou, P. M. Ajayan, Q. Chen, T. Zhu and J. Lou, *Adv. Mater.*, 2017, **29**, 1604201.

75 C. H. Cao, S. Mukherjee, J. Y. Howe, D. D. Perovic, Y. Sun, C. V. Singh and T. Filleter, *Sci. Adv.*, 2018, **4**, eaao7202.

76 I. W. Frank, D. M. Tanenbaum, A. M. van der Zande and P. L. McEuen, *J. Vac. Sci. Technol., B: Microelectron. Nanometer Struct. – Process., Meas., Phenom.*, 2007, **25**, 2558.

77 C. L. Wong, M. Annamalai, Z. Q. Wang and M. Palaniapan, *J. Micromech. Microeng.*, 2010, **20**, 115029.

78 J. U. Lee, D. Yoon and H. Cheong, *Nano Lett.*, 2012, **12**, 4444–4448.

79 M. F. Yu, O. Lourie, M. J. Dyer, K. Moloni, T. F. Kelly and R. S. Ruoff, *Science*, 2000, **287**, 637–640.

80 M. F. Yu, B. S. Files, S. Arepalli and R. S. Ruoff, *Phys. Rev. Lett.*, 2000, **84**, 5552.

81 D. Davidovikj, F. Alijani, S. J. Cartamil-Bueno, H. S. J. van der Zant, M. Amabili and P. G. Steeneken, *Nat. Commun.*, 2017, **8**, 1253.

82 J. Tao, W. F. Shen, S. Wu, L. Liu, Z. H. Feng, C. Wang, C. G. Hu, P. Yao, H. Zhang, W. Pang, X. X. Duan, J. Liu, C. W. Zhou and D. H. Zhang, *ACS Nano*, 2015, **9**, 11362–11370.

83 H. Chen, P. Huang, D. Guo and G. X. Xie, *J. Phys. Chem. C*, 2016, **120**, 29491–29497.

84 K. Liu, Q. M. Yan, M. Chen, W. Fan, Y. H. Sun, J. Suh, D. Y. Fu, S. Lee, J. Zhou, S. Tongay, J. Ji, J. B. Neaton and J. Q. Wu, *Nano Lett.*, 2014, **14**, 5097–5103.

85 A. Castellanos-Gomez, M. Poot, G. A. Steele, H. S. J. van der Zant, N. Agraït and G. Rubio-Bollinger, *Adv. Mater.*, 2012, **24**, 772–775.

86 R. J. T. Nicholl, H. J. Conley, N. V. Lavrik, I. Vlassiouk, Y. S. Puzyrev, V. P. Sreenivas, S. T. Pantelides and K. I. Bolotin, *Nat. Commun.*, 2015, **6**, 8789.

87 C. Gómez-Navarro, M. Burghard and K. Kern, *Nano Lett.*, 2008, **8**, 2045–2049.

88 M. W. Pruessner, T. T. King, D. P. Kelly, R. Grover, L. C. Calhoun and R. Ghodssi, *Sens. Actuators, A*, 2003, **105**, 190–200.

89 S. P. Koenig, N. G. Boddeti, M. L. Dunn and J. S. Bunch, *Nat. Nanotechnol.*, 2011, **6**, 543–546.

90 S. Jiang, S. Shi and X. Wang, *J. Phys. D: Appl. Phys.*, 2014, **47**, 045104.

91 J. G. Simmonds, M. R. Begley and U. Komaragiri, *J. Appl. Mech.*, 2005, **72**, 203–212.

92 L. L. Guo, H. M. Yan, Q. Moore, M. Buettner, J. H. Song, L. Li, P. T. Araujo and H. T. Wang, *Nanoscale*, 2015, **7**, 11915–11921.

93 M. Moreno-Moreno, G. Lopez-Polin, A. Castellanos-Gomez, C. Gomez-Navarro and J. Gomez-Herrero, *2D Mater.*, 2016, **3**, 031007.

94 C. Metzger, S. Rémi, M. Liu, S. V. Kusminskiy, A. H. Castro Neto, A. K. Swan and B. B. Goldberg, *Nano Lett.*, 2010, **10**, 6–10.

95 M. Goldsche, J. Sonntag, T. Khodkov, G. J. Verbiest, S. Reichardt, C. Neumann, T. Ouaj, N. von den Driesch, D. Buca and C. Stampfer, *Nano Lett.*, 2018, **18**, 1707–1713.

96 F. Colangelo, P. Pingue, V. Mišeikis, C. Coletti, F. Beltram and S. Roddaro, *2D Mater.*, 2019, **6**, 025005.

97 Y. Sun, K. Liu, X. Hong, M. Chen, J. Kim, S. Shi, J. Wu, A. Zettl and F. Wang, *Nano Lett.*, 2014, **14**, 5329–5334.

98 P. Manimunda, Y. Nakanishi, Y. M. Jaques, S. Susarla, C. F. Woellner, S. Bhowmick, S. A. S. Asif, D. S. Galvão, C. S. Tiwary and P. M. Ajayan, *2D Mater.*, 2017, **4**, 045005.

99 Y. Li, Z. Hu, S. Lin, S. K. Lai, W. Ji and S. P. Lau, *Adv. Funct. Mater.*, 2017, **27**, 1600986.

100 M. Huang, H. Yan, T. F. Heinz and J. Hone, *Nano Lett.*, 2010, **10**, 4074–4079.

101 P. Lu, X. Wu, W. Guo and X. C. Zeng, *Phys. Chem. Chem. Phys.*, 2012, **14**, 13035–13040.

102 S. Yang, C. Wang, H. Sahin, H. Chen, Y. Li, S. Li, A. Suslu, F. M. Peeters, Q. Liu, J. Li and S. Tongay, *Nano Lett.*, 2015, **15**, 1660–1666.

103 J. W. Suk, R. D. Piner, J. An and R. S. Ruoff, *ACS Nano*, 2010, **4**, 6557–6564.

104 K. N. Spanos, S. K. Georgantzinos and N. K. Anifantis, *Compos. Struct.*, 2015, **132**, 536–544.

105 A. Falin, Q. Cai, E. J. G. Santos, D. Scullion, D. Qian, R. Zhang, Z. Yang, S. Huang, K. Watanabe, T. Taniguchi, M. R. Barnett, Y. Chen, R. S. Ruoff and L. H. Li, *Nat. Commun.*, 2017, **8**, 15815.

106 G. López-Polín, M. Jaafar, F. Guinea, R. Roldán, C. Gómez-Navarro and J. Gómez-Herrero, *Carbon*, 2017, **124**, 42–48.

107 R. Grantab, V. B. Shenoy and R. S. Ruoff, *Science*, 2010, **330**, 946–948.

108 Q. X. Pei, Y. W. Zhang and V. B. Shenoy, *Carbon*, 2010, **48**, 898–904.

109 Q. X. Pei, Y. W. Zhang and V. B. Shenoy, *Nanotechnology*, 2010, **21**, 115709.

110 Y. Pei, *Phys. B*, 2012, **407**, 4436–4439.

111 M. Topsakal, S. Cahangirov and S. Ciraci, *Appl. Phys. Lett.*, 2010, **96**, 091912.

112 Q. Peng, W. Ji and S. De, *Phys. Chem. Chem. Phys.*, 2012, **14**, 13385–13391.

113 Q. Peng, W. Ji and S. De, *Comput. Mater. Sci.*, 2012, **56**, 11–17.

114 E. Torun, H. Sahin, S. Cahangirov, A. Rubio and F. M. Peeters, *J. Appl. Phys.*, 2016, **119**, 074307.

115 Q. Wei and X. Peng, *Appl. Phys. Lett.*, 2014, **104**, 251915.

116 J. H. Zhao, N. Wei, Z. Y. Fan, J. W. Jiang and T. Rabczuk, *Nanotechnology*, 2013, **24**, 095702.

117 Q. Peng and S. De, *Phys. Chem. Chem. Phys.*, 2013, **15**, 19427–19437.

118 L. Xu, N. Wei and Y. Zheng, *Nanotechnology*, 2013, **24**, 505703.

119 C. Carpenter, D. Maroudas and A. Ramasubramaniam, *Appl. Phys. Lett.*, 2013, **103**, 013102.

120 S. Zhao and J. Xue, *J. Phys. D: Appl. Phys.*, 2013, **46**, 135303.

121 A. H. C. Neto, F. Guinea, N. M. R. Peres, K. S. Novoselov and A. K. Geim, *Rev. Mod. Phys.*, 2009, **81**, 109.

122 G. López-Polín, C. Gómez-Navarro, V. Parente, F. Guinea, M. I. Katsnelson, F. Pérez-Murano and J. Gómez-Herrero, *Nat. Phys.*, 2015, **11**, 26–31.

123 F. Hao, D. Fang and Z. Xu, *Appl. Phys. Lett.*, 2011, **99**, 041901.

124 N. K. Perkgöz and C. Sevik, *Nanotechnology*, 2014, **25**, 185701.

125 J. Hou, Z. N. Yin, Y. Y. Zhang and T. C. Chang, *Acta Mech. Sin.*, 2016, **32**, 684–689.

126 J. X. Qu, H. W. Zhang, J. X. Li, S. X. Zhao and T. Chang, *Carbon*, 2017, **120**, 350–357.

127 J. Hou, Z. N. Yin, Y. Y. Zhang and T. Chang, *J. Appl. Mech.*, 2015, **82**, 094501.

128 Y. Y. Zhang, Q. X. Pei and C. M. Wang, *Appl. Phys. Lett.*, 2012, **101**, 081909.

129 J. O. Sofo, A. S. Chaudhari and G. D. Barber, *Phys. Rev. B: Condens. Matter Mater. Phys.*, 2007, **75**, 153401.

130 P. Vogt, P. D. Padova, C. Quaresima, J. Avila, E. Frantzeskakis, M. C. Asensio, A. Resta, B. Ealet and G. L. Lay, *Phys. Rev. Lett.*, 2012, **108**, 155501.

131 S. Rudorf and T. A. Hare, *Superlattices Microstruct.*, 2014, **65**, 64–70.

132 Z. D. Sha, Q. X. Pei, Z. W. Ding, J. W. Jiang and Y. W. Zhang, *J. Phys. D: Appl. Phys.*, 2015, **48**, 395303.

133 L. Song, L. J. Ci, H. Lu, P. B. Sorokin, C. H. Jin, J. Ni, A. G. Kvashnin, D. G. Kvashnin, J. Lou, B. I. Yakobson and P. M. Ajayan, *Nano Lett.*, 2010, **10**, 3209–3215.

134 J. W. Jiang and H. S. Park, *Nat. Commun.*, 2014, **5**, 4727.

135 S. Thomas, K. M. Ajith and V. Cheruvalath, *Mater. Res. Express*, 2017, **4**, 065005.

136 S. Thomas, K. M. Ajith and M. C. Valsakumar, *J. Phys.: Condens. Matter*, 2016, **28**, 295302.

137 G. H. Lee, Y. J. Yu, X. Cui, N. Petrone, C. H. Lee, M. S. Choi, D. Y. Lee, C. Lee, W. J. Yoo, K. Watanabe, T. Taniguchi, C. Nuckolls, P. Kim and J. Hone, *ACS Nano*, 2013, **7**, 7931–7936.

138 Z. Q. Zheng, T. M. Zhang, J. Yao, Y. Zhang, J. Xu and G. W. Yang, *Nanotechnology*, 2016, **27**, 225501.

139 L. Cheng, W. J. Huang, Q. F. Gong, C. H. Liu, Z. Liu, Y. G. Li and H. J. Dai, *Angew. Chem., Int. Ed.*, 2014, **53**, 7860–7863.

140 C. Xu, L. B. Wang, Z. B. Liu, L. Chen, J. K. Guo, N. Kang, X. L. Ma, H. M. Cheng and W. C. Ren, *Nat. Mater.*, 2015, **14**, 1135–1141.

141 T. Li, *Phys. Rev. B: Condens. Matter Mater. Phys.*, 2012, **85**, 235407.

142 S. Bertolazzi, J. Brivio and A. Kis, *ACS Nano*, 2011, **5**, 9703–9709.

143 J. L. Feldman, *J. Phys. Chem. Solids*, 1976, **37**, 1141–1144.

144 B. Mortazavi, M. Shahrokhi, M. Makaremi and T. Rabczuk, *Nanotechnology*, 2017, **28**, 115705.

145 J. W. Jiang and H. S. Park, *Appl. Phys. Lett.*, 2014, **105**, 033108.

146 J. Y. Chung, V. Sorkin, Q. X. Pei, C. H. Chiu and Y. W. Zhang, *J. Phys. D: Appl. Phys.*, 2017, **50**, 345302.

147 A. A. Griffith, *Philos. Trans. R. Soc. London*, 1921, **221**, 163–198.

148 S. W. Cranford and M. J. Buehler, *Carbon*, 2011, **49**, 4111–4121.

149 P. R. Budarapu, B. Javvaji, V. K. Sutrakar, D. R. Mahapatra, M. Paggi, G. Zi and T. Rabczuk, *Int. J. Fract.*, 2017, **203**, 81–98.

150 K. Kim, V. I. Artyukhov, W. Regan, Y. Y. Liu, M. F. Crommie, B. I. Yakobson and A. Zettl, *Nano Lett.*, 2012, **12**, 293–297.

151 C. A. Marianetti and H. G. Yevick, *Phys. Rev. Lett.*, 2010, **105**, 245502.

152 F. Liu, P. Ming and J. Li, *Phys. Rev. B: Condens. Matter Mater. Phys.*, 2007, **76**, 064120.

153 H. D. Wang, X. X. Li, P. Li and J. L. Yang, *Nanoscale*, 2017, **9**, 850–855.

154 F. Traversi, F. J. Gúzman-Vázquez, L. G. Rizzi, V. Russo, C. S. Casari, C. Gómez-Navarro and R. Sordan, *New J. Phys.*, 2010, **12**, 023034.

155 G. H. Lee, R. C. Cooper, S. J. An, S. Lee, A. van der Zande, N. Petrone, A. G. Hammerberg, C. Lee, B. Crawford, W. Oliver, J. W. Kysar and J. Hone, *Science*, 2013, **340**, 1073–1076.

156 Y. Y. Zhang, C. M. Wang, Y. Cheng and Y. Xiang, *Carbon*, 2011, **49**, 4511–4517.

157 K. N. Kudin, G. E. Scuseria and B. I. Yakobson, *Phys. Rev. B: Condens. Matter Mater. Phys.*, 2001, **64**, 235406.

158 H. Șahin, S. Cahangirov, M. Topsakal, E. Bekaroglu, E. Akturk, R. T. Senger and S. Ciraci, *Phys. Rev. B: Condens. Matter Mater. Phys.*, 2009, **80**, 155453.

159 R. C. Andrew, R. E. Mapasha, A. M. Ukpong and N. Chetty, *Phys. Rev. B: Condens. Matter Mater. Phys.*, 2012, **85**, 125428.

160 C. H. Cao, M. Daly, C. V. Singh, Y. Sun and T. Filleter, *Carbon*, 2015, **81**, 497–504.

161 L. Z. Liu, J. F. Zhang, J. J. Zhao and F. Liu, *Nanoscale*, 2012, **4**, 5910–5916.

162 Q. X. Pei, Z. D. Sha, Y. Y. Zhang and Y. W. Zhang, *J. Appl. Phys.*, 2014, **115**, 023519.

163 H. Zhao, *Phys. Lett. A*, 2012, **376**, 3546–3550.

164 Q. Peng, X. Wen and S. De, *RSC Adv.*, 2013, **3**, 13772–13781.

165 J. W. Jiang and H. S. Park, *J. Phys. D: Appl. Phys.*, 2014, **47**, 385304.

166 L. Q. Wang, A. Kutana, X. L. Zou and B. I. Yakobson, *Nanoscale*, 2015, **7**, 9746–9751.

167 Q. L. Xiong, Z. H. Li and X. G. Tian, *J. Phys. D: Appl. Phys.*, 2015, **48**, 375502.

168 B. Mortazavi and Y. Rémond, *Physica E*, 2012, **44**, 1846–1852.

169 T. Han, Y. Luo and C. Wang, *J. Phys. D: Appl. Phys.*, 2014, **47**, 25303.

170 J. T. Wu, B. L. Wang, Y. J. Wei, R. G. Yang and M. Dresselhaus, *Mater. Res. Lett.*, 2013, **1**, 200–206.

171 J. W. Jiang, *Nanotechnology*, 2015, **26**, 315706.

172 A. Kumar and P. K. Ahluwalia, *Physica B*, 2013, **419**, 66–75.

173 Y. Tong, F. J. Yi, L. S. Liu, P. C. Zhai and Q. J. Zhang, *Physica B*, 2010, **405**, 3190–3194.

174 L. C. He, S. Guo, J. C. Lei, Z. D. Sha and Z. S. Liu, *Carbon*, 2014, **75**, 124–132.

175 Y. Y. Liu, F. B. Xu, Z. Zhang, E. S. Penev and B. I. Yakobson, *Nano Lett.*, 2014, **14**, 6782–6786.

176 W. Zhou, X. L. Zou, S. Najmaei, Z. Liu, Y. M. Shi, J. Kong, J. Lou, P. M. Ajayan, B. I. Yakobson and J. C. Idrobo, *Nano Lett.*, 2013, **13**, 2615–2622.

177 O. V. Yazyev and S. G. Louie, *Phys. Rev. B: Condens. Matter Mater. Phys.*, 2010, **81**, 195420.

178 X. L. Zou, Y. Y. Liu and B. I. Yakobson, *Nano Lett.*, 2013, **13**, 253–258.

179 Y. Y. Liu, X. L. Zou and B. I. Yakobson, *ACS Nano*, 2012, **6**, 7053–7058.

180 Y. J. Wei, J. T. Wu, H. Q. Yin, X. H. Shi, R. G. Yang and M. Dresselhaus, *Nat. Mater.*, 2012, **11**, 759–763.

181 Z. G. Song, V. I. Artyukhov, B. I. Yakobson and Z. P. Xu, *Nano Lett.*, 2013, **13**, 1829–1833.

182 K. Q. Dang and D. E. Spearot, *J. Appl. Phys.*, 2014, **116**, 013508.

183 S. Eigler, M. Enzelberger-Heim, S. Grimm, P. Hofmann, W. Kroener, A. Geworski, C. Dotzer, M. Röckert, J. Xiao, C. Papp, O. Lytken, H. P. Steinrück, P. Müller and A. Hirsch, *Adv. Mater.*, 2013, **25**, 3583–3587.

184 R. T. Lv, J. A. Robinson, R. E. Schaak, D. Sun, Y. F. Sun, T. E. Mallouk and M. Terrones, *Acc. Chem. Res.*, 2015, **48**, 56–64.

185 Y. Lu, B. R. Goldsmith, N. J. Kybert and A. T. C. Johnson, *Appl. Phys. Lett.*, 2010, **97**, 083107.

186 P. K. Kannan, D. J. Late, H. Morgan and C. S. Rout, *Nanoscale*, 2015, **7**, 13293–13312.

187 W. W. Cai, R. D. Piner, F. J. Stadermann, S. Park, M. A. Shaibat, Y. Ishii, D. X. Yang, A. Velamakanni, S. J. An, M. Stoller, J. An, D. M. Chen and R. S. Ruoff, *Science*, 2008, **321**, 1815–1817.

188 J. C. Meyer, A. K. Geim, M. I. Katsnelson, K. S. Novoselov, T. J. Booth and S. Roth, *Nature*, 2007, **446**, 60–63.

189 J. Brivio, D. T. L. Alexander and A. Kis, *Nano Lett.*, 2011, **11**, 5148–5153.

190 H. X. Zhang and P. X. Feng, *ACS Appl. Mater. Interfaces*, 2012, **4**, 30–33.

191 Z. T. Luo, Y. Lu, D. W. Singer, M. E. Berck, L. A. Somers, B. R. Goldsmith and A. T. C. Johnson, *Chem. Mater.*, 2011, **23**, 1441–1447.

192 K. K. Kim, A. Hsu, X. T. Jia, S. M. Kim, Y. M. Shi, M. Hofmann, D. Nezich, J. F. Rodriguez-Nieva, M. Dresselhaus, T. Palacios and J. Kong, *Nano Lett.*, 2012, **12**, 161–166.

193 R. Y. Tay, M. H. Griep, G. Mallick, S. H. Tsang, R. S. Singh, T. Tumlin, E. H. T. Teo and S. P. Karna, *Nano Lett.*, 2014, **14**, 839–846.

194 K. H. Lee, H. J. Shin, J. Lee, I. Lee, G. H. Kim, J. Y. Choi and S. W. Kim, *Nano Lett.*, 2012, **12**, 714–718.

195 B. Zhang, W. H. Lee, R. Piner, I. Kholmanov, Y. P. Wu, H. F. Li, H. X. Ji and R. S. Ruoff, *ACS Nano*, 2012, **6**, 2471–2476.

196 M. H. Griep, E. Sandoz-Rosado, T. M. Tumlin and E. Wetzel, *Nano Lett.*, 2016, **16**, 1657–1662.

197 J. O. Island, G. A. Steele, H. S. J. van der Zant and A. Castellanos-Gomez, *2D Mater.*, 2015, **2**, 011002.

198 J. D. Wood, S. A. Wells, D. Jariwala, K. S. Chen, E. Cho, V. K. Sangwan, X. L. Liu, L. J. Lauhon, T. J. Marks and M. C. Hersam, *Nano Lett.*, 2014, **14**, 6964–6970.

199 Z. Wang, L. Philippe and J. Elias, *Phys. Rev. B: Condens. Matter Mater. Phys.*, 2010, **81**, 155405.

200 Z. Wang, *Carbon*, 2009, **47**, 3050–3053.

201 Z. Osváth, F. Lefloch, V. Bouchiat and C. Chapelier, *Nanoscale*, 2013, **5**, 10996–11002.

202 P. Hao, Y. W. Gao and Y. H. Zhou, *Sci. China: Phys., Mech. Astron.*, 2013, **56**, 1148–1156.

203 Q. Lu and R. Huang, *Int. J. Appl. Mech.*, 2009, **1**, 443–467.

204 P. Huang, D. Guo, G. X. Xie and J. Li, *Nano Lett.*, 2017, **17**, 6280–6286.

205 V. M. Pereira and A. H. C. Neto, *Phys. Rev. Lett.*, 2009, **103**, 046801.

206 F. Guinea, M. I. Katsnelson and A. K. Geim, *Nat. Phys.*, 2010, **6**, 30–33.

207 A. Castellanos-Gomez, R. Roldán, E. Cappelluti, M. Buscema, F. Guinea, H. S. J. van der Zant and G. A. Steele, *Nano Lett.*, 2013, **13**, 5361–5366.

208 A. P. Nayak, S. Bhattacharyya, J. Zhu, J. Liu, X. Wu, T. Pandey, C. Q. Jin, A. K. Singh, D. Akinwande and J. F. Lin, *Nat. Commun.*, 2014, **5**, 3731.

209 L. Kou, C. Tang, W. Guo and C. Chen, *ACS Nano*, 2011, **5**, 1012–1017.

210 Y. Ma, Y. Dai, M. Guo, C. Niu, L. Yu and B. Huang, *Nanoscale*, 2011, **3**, 2301–2306.

211 Y. D. Ma, Y. Dai, M. Guo, C. W. Niu, Y. T. Zhu and B. B. Huang, *ACS Nano*, 2012, **6**, 1695–1701.

212 A. D. Smith, F. Niklaus, A. Paussa, S. Schröder, A. C. Fischer, M. Sterner, S. Wagner, S. Vaziri, F. Forsberg, D. Esseni, M. Östling and M. C. Lemme, *ACS Nano*, 2016, **10**, 9879–9886.

213 A. D. Smith, F. Niklaus, A. Paussa, S. Vaziri, A. C. Fischer, M. Sterner, F. Forsberg, A. Delin, D. Esseni, P. Palestri, M. Östling and M. C. Lemme, *Nano Lett.*, 2013, **13**, 3237–3242.

214 X. W. Fu, Z. M. Liao, J. X. Zhou, Y. B. Zhou, H. C. Wu, R. Zhang, G. Jing, J. Xu, X. Wu, W. Guo and D. Yu, *Appl. Phys. Lett.*, 2011, **99**, 213107.

215 S. Manzeli, A. Allain, A. Ghadimi and A. Kis, *Nano Lett.*, 2015, **15**, 5330–5335.

216 Z. Zhang, L. Li, J. Horng, N. Z. Wang, F. Yang, Y. Yu, Y. Zhang, G. Chen, K. Watanabe, T. Taniguchi, X. H. Chen, F. Wang and Y. Zhang, *Nano Lett.*, 2017, **17**, 6097–6103.

217 C. An, Z. Xu, W. Shen, R. Zhang, Z. Sun, S. Tang, Y. Xiao, D. Zhang, D. Sun, X. Hu, C. Hu, L. Yang and J. Liu, *ACS Nano*, 2019, **13**, 3310–3319.

218 X. D. Wang, J. Zhou, J. H. Song, J. Liu, N. S. Xu and Z. L. Wang, *Nano Lett.*, 2006, **6**, 2768–2772.

219 R. Yang, Y. Qin, L. Dai and Z. L. Wang, *Nat. Nanotechnol.*, 2009, **4**, 34–39.

220 K. H. Michel and B. Verberck, *Phys. Rev. B: Condens. Matter Mater. Phys.*, 2009, **80**, 224301.

221 K. A. N. Duerloo, M. T. Ong and E. J. Reed, *J. Phys. Chem. Lett.*, 2012, **3**, 2871–2876.

222 R. X. Fei, W. B. Li, J. Li and L. Yang, *Appl. Phys. Lett.*, 2015, **107**, 173104.

223 H. L. Zhuang, M. D. Johannes, M. N. Blonsky and R. G. Hennig, *Appl. Phys. Lett.*, 2014, **104**, 022116.

224 M. N. Blonsky, H. L. Zhuang, A. K. Singh and R. G. Hennig, *ACS Nano*, 2015, **9**, 9885–9891.

225 M. T. Ong and E. J. Reed, *ACS Nano*, 2012, **6**, 1387–1394.

226 X. Wang, H. Tian, W. Xie, Y. Shu, W. T. Mi, M. A. Mohammad, Q. Y. Xie, Y. Yang, J. B. Xu and T. L. Ren, *NPG Asia Mater.*, 2015, **7**, e154.

227 G. da Cunha Rodrigues, P. Zelenovskiy, K. Romanyuk, S. Luchkin, Y. Kopelevich and A. Kholkin, *Nat. Commun.*, 2015, **6**, 7572.

228 W. Z. Wu, L. Wang, Y. L. Li, F. Zhang, L. Lin, S. M. Niu, D. Chenet, X. Zhang, Y. F. Hao, T. F. Heinz, J. Hone and Z. L. Wang, *Nature*, 2014, **514**, 470–474.

229 H. Zhu, Y. Wang, J. Xiao, M. Liu, S. Xiong, Z. J. Wong, Z. Ye, Y. Ye, X. Yin and X. Zhang, *Nat. Nanotechnol.*, 2015, **10**, 151–155.

230 S. K. Kim, R. Bhatia, T. H. Kim, D. Seol, J. H. Kim, H. Kim, W. Seung, Y. Kim, Y. H. Lee and Sa. W. Kim, *Nano Energy*, 2016, **22**, 483–489.

231 E. N. Esfahani, T. Li, B. Huang, X. Xu and J. Li, *Nano Energy*, 2018, **52**, 117–122.

232 J. H. Lee, J. Y. Park, E. B. Cho, T. Y. Kim, S. A. Han, T. H. Kim, Y. Liu, S. K. Kim, C. J. Roh, H. J. Yoon, H. Ryu, W. Seung, J. S. Lee, J. Lee and S. W. Kim, *Adv. Mater.*, 2017, **29**, 1606667.

233 R. R. Nair, P. Blake, A. N. Grigorenko, K. S. Novoselov, T. J. Booth, T. Stauber, N. M. R. Peres and A. K. Geim, *Science*, 2008, **320**, 1308–1308.

234 V. M. Pereira, R. M. Ribeiro, N. M. R. Peres and A. H. C. Neto, *Europhys. Lett.*, 2011, **92**, 67001.

235 G. X. Ni, H. Z. Yang, W. Ji, S. J. Baeck, C. T. Toh, J. H. Ahn, V. M. Pereira and B. Özyilmaz, *Adv. Mater.*, 2014, **26**, 1081–1086.

236 M. O. Leyva and G. G. Naumis, *2D Mater.*, 2015, **2**, 025001.

237 F. Kafi, R. P. Shahri, M. R. Benam and A. Akhtar, *J. Electron. Mater.*, 2017, **46**, 6158–6166.

238 S. Deng, Y. Zhang and L. Li, *Appl. Surf. Sci.*, 2019, **476**, 308–316.

239 A. C. Ferrari, J. C. Meyer, V. Scardaci, C. Casiraghi, M. Lazzeri, F. Mauri, S. Piscanec, D. Jiang, K. S. Novoselov, S. Roth and A. K. Geim, *Phys. Rev. Lett.*, 2006, **97**, 187401.

240 O. Frank, G. Tsoukleri, J. Parthenios, K. Papagelis, I. Riaz, R. Jalil, K. S. Novoselov and C. Galiotis, *ACS Nano*, 2010, **4**, 3131–3138.

241 T. M. G. Mohiuddin, A. Lombardo, R. R. Nair, A. Bonetti, G. Savini, R. Jalil, N. Bonini, D. M. Basko, C. Galiotis, N. Marzari, K. S. Novoselov, A. K. Geim and A. C. Ferrari, *Phys. Rev. B: Condens. Matter Mater. Phys.*, 2009, **79**, 205433.

242 O. Frank, M. Mohr, J. Maultzsch, C. Thomsen, I. Riaz, R. Jalil, K. S. Novoselov, G. Tsoukleri, J. Parthenios, K. Papagelis, L. Kavan and C. Galiotis, *ACS Nano*, 2011, **5**, 2231–2239.

243 M. Huang, H. Yan, C. Chen, D. Song, T. F. Heinz and J. Hone, *Proc. Natl. Acad. Sci. U. S. A.*, 2009, **106**, 7304–7308.

244 M. Yagmurcukardes, C. Bacaksiz, E. Unsal, B. Akbali, R. T. Senger and H. Sahin, *Phys. Rev. B: Condens. Matter Mater. Phys.*, 2018, **97**, 115427.

245 T. J. Wieting and J. L. Verble, *Phys. Rev. B: Condens. Matter Mater. Phys.*, 1971, **3**, 4286.

246 J. M. Chen and C. S. Wang, *Solid State Commun.*, 1974, **14**, 857–860.

247 Y. Wang, C. Cong, C. Qiu and T. Yu, *Small*, 2013, **9**, 2857–2861.

248 C. Rice, R. J. Young, R. Zan and U. Bangert, *Phys. Rev. B: Condens. Matter Mater. Phys.*, 2013, **87**, 081307.

249 H. J. Conley, B. Wang, J. I. Ziegler, R. F. Haglund Jr., S. T. Pantelides and K. I. Bolotin, *Nano Lett.*, 2013, **13**, 3626–3630.

250 Y. Wang, C. Cong, W. Yang, J. Shang, N. Peimyoo, Y. Chen, J. Kang, J. Wang, W. Huang and T. Yu, *Nano Res.*, 2015, **8**, 2562–2572.

251 S. Sugai and I. Shirotani, *Solid State Commun.*, 1985, **53**, 753–755.

252 X. Ling, L. Liang, S. Huang, A. A. Puretzky, D. B. Geohegan, B. G. Sumpter, J. Kong, V. Meunier and M. S. Dresselhaus, *Nano Lett.*, 2015, **15**, 4080–4088.

253 J. X. Wu, N. N. Mao, L. M. Xie, H. Xu and J. Zhang, *Angew. Chem., Int. Ed.*, 2015, **54**, 2366–2369.

254 H. B. Ribeiro, M. A. de Pimenta, C. J. S. de Matos, R. L. Moreira, A. S. Rodin, J. D. Zapata, E. A. T. de Souza and A. H. Castro Neto, *ACS Nano*, 2015, **9**, 4270–4276.

255 Y. Wang, C. Cong, R. Fei, W. Yang, Y. Chen, B. Cao, L. Yang and T. Yu, *Nano Res.*, 2015, **8**, 3944–3953.

256 S. Zhang, N. Mao, J. Wu, L. Tong, J. Zhang and Z. Liu, *Small*, 2017, **13**, 1700466.

257 H. Zhao and N. R. Aluru, *J. Appl. Phys.*, 2010, **108**, 064321.

258 S. Chen and D. C. Chrzan, *Phys. Rev. B: Condens. Matter Mater. Phys.*, 2011, **84**, 195409.

259 W. Gao and R. Huang, *J. Mech. Phys. Solids*, 2014, **66**, 42–58.

260 K. A. N. Duerloo, Y. Li and E. J. Reed, *Nat. Commun.*, 2014, **5**, 4214.

261 J. A. Wilson and A. D. Yoffe, *Adv. Phys.*, 1969, **18**, 193–335.

262 H. H. Huang, X. Fan, D. J. Singh, H. Chen, Q. Jiang and W. T. Zheng, *Phys. Chem. Chem. Phys.*, 2016, **18**, 4086–4094.

263 S. Song, D. H. Keum, S. Cho, D. Perello, Y. Kim and Y. H. Lee, *Nano Lett.*, 2016, **16**, 188–193.

264 X. Qian, J. Liu, L. Fu and J. Li, *Science*, 2014, **346**, 1344–1347.

265 Y. Ma, L. Kou, X. Li, Y. Dai and T. Heine, *Phys. Rev. B: Condens. Matter Mater. Phys.*, 2016, **93**, 035442.

266 F. Ma, G. Gao, Y. Jiao, Y. Gu, A. Bilic, H. Zhang, Z. Chen and A. Du, *Nanoscale*, 2016, **8**, 4969–4975.

267 X. Li, S. Zhang and Q. Wang, *Nanoscale*, 2017, **9**, 562–569.

268 E. T. Sisakht, F. Fazileh, M. H. Zare, M. Zarenia and F. M. Peeters, *Phys. Rev. B: Condens. Matter Mater. Phys.*, 2016, **94**, 085417.

269 T. Zhang, J. H. Lin, Y. M. Yu, X. R. Chen and W. M. Liu, *Sci. Rep.*, 2015, **5**, 13927.

270 T. Hu and J. Dong, *Phys. Rev. B: Condens. Matter Mater. Phys.*, 2015, **92**, 064114.

271 D. Akinwande, N. Petrone and J. Hone, *Nat. Commun.*, 2014, **5**, 5678.

272 C. Lee, Q. Y. Li, W. Kalb, X. Z. Liu, H. Berger, R. W. Carpick and J. Hone, *Science*, 2010, **328**, 76–80.

273 J. Yoon, W. Park, G. Y. Bae, Y. Kim, H. S. Jang, Y. Hyun, S. K. Lim, Y. H. Kahng, W. K. Hong, B. H. Lee and H. C. Ko, *Small*, 2013, **9**, 3295–3300.

274 S. Das, R. Gulotty, A. V. Sumant and A. Roelofs, *Nano Lett.*, 2014, **14**, 2861–2866.

275 J. Lee, L. Tao, K. N. Parrish, Y. F. Hao, R. S. Ruoff and D. Akinwande, *Appl. Phys. Lett.*, 2012, **101**, 252109.

276 J. Lee, T. J. Ha, H. F. Li, K. N. Parrish, M. Holt, A. Dodabalapur, R. S. Ruoff and D. Akinwand, *ACS Nano*, 2013, **7**, 7744–7750.

277 J. S. Qiao, X. H. Kong, Z. X. Hu, F. Yang and W. Ji, *Nat. Commun.*, 2014, **5**, 4475.

278 H. Y. Chang, S. X. Yang, J. Lee, L. Tao, W. S. Hwang, D. Jena, N. S. Lu and D. Akinwande, *ACS Nano*, 2013, **7**, 5446–5452.

279 W. N. Zhu, M. N. Yogeesh, S. X. Yang, S. H. Aldave, J. S. Kim, S. Sonde, L. Tao, N. S. Lu and D. Akinwande, *Nano Lett.*, 2015, **15**, 1883–1890.

280 T. Q. Trung, N. T. Tien, D. Kim, M. Jang, O. J. Yoon and N. E. Lee, *Adv. Funct. Mater.*, 2014, **24**, 117–124.

281 Y. Wang, L. Wang, T. Yang, X. Li, X. Zang, M. Zhu, K. Wang, D. Wu and H. Zhu, *Adv. Funct. Mater.*, 2014, **24**, 4666–4670.

282 M. Park, Y. J. Park, X. Chen, Y. K. Park, M. S. Kim and J. H. Ahn, *Adv. Mater.*, 2016, **28**, 2556–2562.

283 W. Feng, W. Zheng, F. Gao, X. S. Chen, G. Liu, T. Hasan, W. W. Cao and P. A. Hu, *Chem. Mater.*, 2016, **28**, 4278–4283.

284 Y. Wang, R. Yang, Z. Shi, L. Zhang, D. Shi, E. Wang and G. Zhang, *ACS Nano*, 2011, **5**, 3645–3650.

285 X. Li, R. Zhang, W. Yu, K. Wang, J. Wei, D. Wu, A. Cao, Z. Li, Y. Cheng, Q. Zheng, R. S. Ruoff and H. Zhu, *Sci. Rep.*, 2012, **2**, 870.

286 Y. Lee, S. Bae, H. Jang, S. Jang, S. E. Zhu, S. H. Sim, Y. L. Song, B. H. Hong and J. H. Ahn, *Nano Lett.*, 2010, **10**, 490–493.

287 S. H. Bae, Y. Lee, B. K. Sharma, H. J. Lee, J. H. Kim and J. H. Ahn, *Carbon*, 2013, **51**, 236–242.

288 J. Zhao, C. He, R. Yang, Z. Shi, M. Cheng, W. Yang, G. Xie, D. Wang, D. Shi and G. Zhang, *Appl. Phys. Lett.*, 2012, **101**, 063112.

289 J. Zhao, G. Wang, R. Yang, X. Lu, M. Cheng, C. He, G. Xie, J. Meng, D. Shi and G. Zhang, *ACS Nano*, 2015, **9**, 1622–1629.

290 X. Li, T. Yang, Y. Yang, J. Zhu, Li. Li, F. E. Alam, X. Li, K. Wang, H. Cheng, C. T. Lin, Y. Fang and H. Zhu, *Adv. Funct. Mater.*, 2016, **26**, 1322–1329.

291 J. J. Park, W. J. Hyun, S. C. Mun, Y. T. Park and O. O. Park, *ACS Appl. Mater. Interfaces*, 2015, **7**, 6317–6324.

292 S. Chun, Y. Choi and W. Park, *Carbon*, 2017, **116**, 753–759.

293 M. Y. Tsai, A. Tarasov, Z. R. Hesabi, H. Taghinejad, P. M. Campbell, C. A. Joiner, A. Adibi and E. M. Vogel, *ACS Appl. Mater. Interfaces*, 2015, **7**, 12850–12855.

294 S. Wagner, C. Yim, N. McEvoy, S. Kataria, V. Yokaribas, A. Kuc, S. Pindl, C. P. Fritzen, T. Heine, G. S. Duesberg and M. C. Lemme, *Nano Lett.*, 2018, **18**, 3738–3745.

295 S. A. Han, T. H. Kim, S. K. Kim, K. H. Lee, H. J. Park, J. H. Lee and S. W. Kim, *Adv. Mater.*, 2018, **30**, 1800342.

296 W. Wu, L. Wang, R. Yu, Y. Liu, S. H. Wei, J. Hone and Z. L. Wang, *Adv. Mater.*, 2016, **28**, 8463–8468.

297 J. Qi, Y. W. Lan, A. Z. Stieg, J. H. Chen, Y. L. Zhong, L. J. Li, C. D. Chen, Y. Zhang and K. L. Wang, *Nat. Commun.*, 2015, **6**, 7430.

298 X. Wang, X. He, H. Zhu, L. Sun, W. Fu, X. Wang, L. C. Hoong, H. Wang, Q. Zeng, W. Zhao, J. Wei, Z. Jin, Z. Shen, J. Liu, T. Zhang and Z. Liu, *Sci. Adv.*, 2016, **2**, e1600209.

299 P. Kang, M. C. Wang, P. M. Knapp and S. W. Nam, *Adv. Mater.*, 2016, **28**, 4639–4645.

300 M. Kim, P. Kang, J. Leem and S. W. Nam, *Nanoscale*, 2017, **9**, 4058–4065.

301 J. D. Zhou, J. H. Lin, X. W. Huang, Y. Zhou, Y. Chen, J. Xia, H. Wang, Y. Xie, H. M. Yu, J. C. Lei, D. Wu, F. C. Liu, Q. D. Fu, Q. S. Zeng, C. H. Hsu, C. L. Yang, L. Lu, T. Yu, Z. X. Shen, H. Lin, B. I. Yakobson, Q. Liu, K. Suenaga, G. T. Liu and Z. Liu, *Nature*, 2018, **556**, 355–359.

302 H. Hosseinzadegan, C. Todd, A. Lal, M. Pandey, M. Levendorf and J. Park, 2012 IEEE 25th international conference on micro electro mechanical systems, 2012, pp. 611–614.

303 S. E. Zhu, M. K. Ghatkesar, C. Zhang and G. C. A. M. Janssen, *Appl. Phys. Lett.*, 2013, **102**, 161904.

304 H. Tian, Y. Shu, Y. L. Cui, W. T. Mi, Y. Yang, D. Xie and T. L. Ren, *Nanoscale*, 2014, **6**, 699–705.

305 Q. Wang, W. Hong and L. Dong, *Nanoscale*, 2016, **8**, 7663–7671.